Cryo-electron tomography sheds light on the elastic nature of the *Trypanosoma brucei* tripartite attachment complex

Irina Bregy[1,2,3], Julika Radecke[4], Akira Noga[5], Hugo van den Hoek[6], Mara Kern[1], Beat Haenni[2], Benjamin D. Engel[6], C. Alistair Siebert[4], Takashi Ishikawa[5,7], Benoît Zuber[2#], Torsten Ochsenreiter[1#]

[#]corresponding author

[1]Institute of Cell Biology, University of Bern, Baltzerstrasse 4, Bern CH-3012, Switzerland;

[2]Institute of Anatomy, University of Bern, Baltzerstrasse 2, Bern CH-3012, Switzerland;

[3]Graduate School for Cellular and Biomedical Sciences, Freiestrasse 1, Bern CH-3012, Switzerland;

[4]Electron Bio-Imaging Centre, Diamond Light Source, Oxfordshire OX11 0DE, Didcot, United Kingdom;

[5]Division of Biology and Chemistry, Paul Scherrer Institute, Forschungsstrasse 111, Villigen CH-5232, Switzerland

[6]Biozentrum, University of Basel, Spitalstrasse 41, Basel CH-4056, Switzerland

[7]Department of Biology, ETH Zurich, Zurich, Switzerland

Corresponding Authors:

Torsten Ochsenreiter, Baltzerstrasse 4, Institute of Cell Biology, University of Bern, Switzerland, torsten.ochsenreiter@unibe.ch

Benoît Zuber, Baltzerstrasse 2, Institute of Anatomy, University of Bern, Switzerland, benoit.zuber@unibe.ch

Keywords

Cryo-electron tomography (cryo-ET), tripartite attachment complex (TAC), molecular spring, mitochondrial genome anchoring, mitochondrial genome segregation, kDNA, *Trypanosoma brucei*

Abstract

In contrast to many eukaryotic organisms, trypanosomes only contain a single mitochondrion per cell. Within that singular mitochondrion, the protist carries a single mitochondrial genome that consists of a complex DNA network, the kinetoplast DNA (kDNA). Segregation of the replicated kDNA is coordinated by the basal body of the cell's single flagellum. The tripartite attachment complex (TAC) forms a physical connection between the proximal end of the basal body and the kDNA. This allows anchoring of the kDNA throughout the cell cycle and couples kDNA segregation with the separation of the basal bodies prior to cell division. Over the past years, several components of the TAC have been identified. To shed light on the structure of the cytoplasmic part of the TAC (known as the exclusion zone), we performed cryo-electron tomography on whole cells. This allowed us to acquire three-dimensional high-resolution images of the exclusion zone *in situ*. We observed that the

exclusion zone filaments offer great mechanical flexibility for basal body movement. We measured the dimensions of the individual structural elements of the area, as well as the overall orientation and positioning of the basal bodies towards the mitochondrial kDNA pocket. Using a combination of experimental data and modelling, we generated a structural model of the exclusion zone protein p197. Our findings suggest that the majority of p197 consists of a string of spectrin-like repeats. We propose that these structural units provide the architecture of a molecular spring and that they are required in the TAC to withstand the mechanical forces generated through basal body repositioning events during kDNA segregation and motility of the organism.

Introduction

The mitochondrion is a hallmark of eukaryotic life and it is responsible for essential processes ranging from catabolic reactions like oxidative phosphorylation, to anabolic processes such as iron-sulfur cluster assembly (Braymer & Lill, 2017; Friedman & Nunnari, 2014). Many mitochondrial genes have been transferred to the nucleus, and thus the encoded proteins are produced in the cytoplasm and imported into the mitochondrion. Some essential genes, however, remain encoded on the mitochondrial genome. Thus, trypanosomes, like most other eukaryotes, depend on the inheritance of an intact mitochondrial genome for their survival.

Along with the other members of the Kinetoplastea, trypanosomes possess one single, large mitochondrion per cell (Tyler et al., 2001). The singular nature of the mitochondrion and mitochondrial genome requires to take special care of replicating and segregating that genome correctly, prior to cytokinesis (Schneider & Ochsenreiter, 2018). Because of their unique mitochondrial biology, trypanosomes evolved a distinct mitochondrial DNA structure, with highly adapted replication and segregation proteins.

The mitochondrial DNA in trypanosomes is condensed to a disc-like network of interlocked circular DNA molecules that are positioned at the posterior end of the cell body (Jensen & Englund, 2012). This structure has been termed the kinetoplast, with its DNA content referred to as the kinetoplast DNA (kDNA) (Trager, 1965). The kDNA consists of two major classes of DNA molecules. The maxicircles (~25 molecules of ~23 kb) encode for cryptogenes that depend on an mRNA editing process to form translatable mRNAs (Hajduk & Ochsenreiter, 2010; Jensen & Englund, 2012; Povelones, 2014). Editing sites on primary mRNAs are recognized by guide RNAs, which are encoded on the ~5000 minicircles (~1kb) (Hong & Simpson, 2003; Ochsenreiter et al., 2007). With the help of guide RNAs, an enzymatic machinery called the editosome can then insert/delete uridine residues from the primary mRNA to form a modified mRNA that encodes for a translatable open reading frame (ORF). Within the kDNA network, minicircles are interlocked with each other and the maxicircles (Chen et al., 1995). With a thickness of about half the circumference of a minicircle, the kDNA dimensions depend on minicircle size, and thus vary among different species of the Kinetoplastea (Jakob et al., 2016; Jensen & Englund, 2012).

Replication of this highly organized DNA network requires the organism to release the individual DNA molecules from catenation to neighboring DNA circles (Jensen & Englund, 2012). The minicircles thus are released from the network prior to replication and move to two opposing poles of the kDNA disc

(known as the antipodal sites) where they are then replicated and reattached to the network (Amodeo et al., 2022; Jensen & Englund, 2012). Maxicircles on the other hand, are believed to remain attached to the network throughout the replication process. Subsequent segregation of the duplicated kDNA is organized by the basal body (BB) of the flagellum (Ogbadoyi et al., 2003; Schneider & Ochsenreiter, 2018). To allow for coupling of kDNA segregation and BB separation prior to cytokinesis, the kDNA remains physically attached to the proximal end of the BB throughout the cell cycle. This connection, spanning the cytosol, the mitochondrial membranes and the mitochondrial matrix, has been termed the tripartite attachment complex (TAC, (Ogbadoyi et al., 2003)). The TAC not only allows for coordinated segregation of the kDNA, but also anchors the kDNA to its position throughout the cell cycle. As the TAC has to bridge three biochemically distinct regions of the cell to reach from the BB to the mitochondrial DNA, it has been subdivided into three substructures: i) the exclusion zone filaments (EZFs) connecting the BB and the pro-basal body (pBB) to the outer mitochondrial membrane (OMM), ii) the differentiated mitochondrial membranes (DMs, containing a unique set of TAC-specific proteins) and iii) the unilateral filaments (ULFs) that span the distance between the inner mitochondrial membrane (IMM) and the kDNA itself (Ogbadoyi et al., 2003).

Over the past decades, several components of the TAC have been identified (Amodeo et al., 2022; Schneider & Ochsenreiter, 2018). While most of them localize to the DMs or the ULFs, it seems that the EZF protein p197 spans the entire exclusion zone (Aeschlimann et al., 2022; Gheiratmand et al., 2013). Its N-terminus localizes at the OMM, while the C-terminus localizes to the proximal end of the BB/ pBB (Aeschlimann et al., 2022). In addition, p197 contains a central section of 26-28 nearly identical repeats of 175-182 amino acids (Aeschlimann et al., 2022; Naguleswaran et al., 2021). Because of its large size, we assume the repeat section to be structurally highly important for the function of p197. p197 stably anchors the BB to the DMs, while tolerating the extensive remodeling processes we observe across the *T. brucei* cell cycle. Interestingly, the amino acid sequence of the ortholog of p197 found in the closely related parasite *Trypanosoma cruzi* (Tcp197) is more than 70 % similar in the terminal domains, but does not contain a repeat section in the middle part of the protein (Aeschlimann et al., 2022). Consequently, the *T. cruzi* protein is much shorter. Experimental replacement of the *T. brucei* p197 repeat section with the corresponding central region of the *T. cruzi* ortholog demonstrates that the *T. cruzi* protein is not able to complement for the function of the repeat section in *T. brucei* p197 (Aeschlimann et al., 2022). This difference in the composition of p197 is also reflected by differences in cell cycle dynamics observed between the two parasites. While the cell cycle of *T. brucei* has been shown to include a rotation of the new BB around the old BB prior to kDNA segregation, a similar process seems not to take place in *T. cruzi* (Elias et al., 2007; Vaughan & Gull, 2016). In fact, *T. cruzi* was shown to delay migration and repositioning of the new BB until after the two daughter cells have been generated asymmetrically (Elias et al., 2007).

To better understand how p197 functions, we investigated the structural organization of the exclusion zone using cryo-electron tomography (cryo-ET). *T. brucei* cells are too thick to be imaged directly by cryo-ET of whole cells. At the TAC region, the average cell is about two micrometers thick. Typically, transmission electron microscopy (TEM) is only feasible for samples with a maximum

thickness of about 500 nm, as thicker samples will yield images of a very low contrast due to inelastic scattering of the electron beam. To circumvent this limitation, we followed two complementary approaches. On the one hand, we thinned the cells before imaging them by cryo-ET; on the other hand, we imaged anucleated cells, which are within the acceptable thickness range. For the first approach we used cryo-focused ion beam (FIB) milling to prepare thin lamellae through vitreously frozen cells (Marko et al., 2007; Schaffer et al., 2017). While very effective in creating thin samples, cryo-FIB milling significantly limits throughput. Therefore, to collect a large dataset, we followed the second approach. As previously demonstrated by Sun and colleagues, anucleated trypanosomes, commonly referred to as zoids, are considerably thinner than their nucleated counterpart and are suitable for cryo-ET (Robinson et al., 1995; Sun et al., 2018).

Results

To get an overview of the TAC structure *in situ*, we performed cryo-ET on vitrified wild type procyclic trypanosomes. We thinned down the sample by cryo-FIB milling. The complete workflow from sample preparation, to tilt-series acquisition and data processing is shown in Figure 1 A and detailed in the materials and methods section. A series of three positions across the z-axis of a tomogram generated with this approach is shown in Figure 2 A. The zoom-in images in Figure 2 B show a magnified view of the TAC area.

The cytosolic and membraneous parts of the TAC are nicely resolved in cryo-ET of cryo-FIB milled *T. brucei* (Figure 2 A). When milled at the corresponding position, the BB, the kDNA pocket of the mitochondrion and the kDNA itself are clearly visible. Furthermore, the EZFs of the TAC are well-resolved and marked in the zoomed images in Figure 2 B (arrowheads).

While the area of interest was well-resolved in the data generated with this method, we decided to only acquire a few data sets using this method, while collecting most of our data using zoids, which are thin enough for whole-cell cryo-ET (Sun et al., 2018). Zoids can be generated through the depletion of TbCentrin4, a protein involved in nuclear division and cytokinesis (Shi et al., 2008; Sun et al., 2018).

Procyclic *T. brucei* cells were transfected with an RNAi construct targeting the ORF of TbCentrin4. Additionally, we generated a TbCentrin4 p197 double RNAi cell line. p197 RNAi causes the disassembly of the entire TAC including the EZFs (Hoffmann et al., 2018). The combination of TbCentrin4 RNAi with the knockdown of p197 generated TAC-depleted zoids (tdzoids) that we used as a control cell line.

The workflow to generate tomographic data on zoid cells is schematically shown in Figure 1 B. To increase the relative number of slim trypanosomes in our sample, we aimed to achieve a high percentage of zoids in the population. As described by Shi and colleagues, TbCentrin4 RNAi only causes a fraction of the population to end up in zoid state (~40 % after 72 h of induction, (Shi et al., 2008)). After expressing the RNAi construct for 65 h, we therefore enriched the TbCentrin4 knockdown population for zoids with a series of centrifugation steps (as described by (Sun et al., 2018)). The final population consisted to 80 % of zoids (distribution of nucleus-/kinetoplast-content shown in Figure 1 C). The enriched zoids where then plunge frozen and imaged by cryo-ET.

The TbCentrin4 p197 double RNAi cell line was treated as were TbCentrin4 RNAi cells. The enrichment resulted in a concentration of 50 % tdzoids in the final population (karyotype distribution in Figure 1 D). While this ratio is considerably lower than the values reached for zoids, it is worth mentioning that only 8 % of the cells in the enriched population retained the kDNA. Thus, the probability of imaging a tdzoid containing an intact TAC was very low.

TbCentrin4 RNAi generates zoids that are suitable for studying the TAC area by cryo-ET

TbCentrin4 localizes to the Golgi-associated bilobe structure and to the BBs (Shi et al., 2008). Hence, the protein also localizes close to the TAC. Because of this spatial proximity, we wanted to exclude any effect on the TAC due to TbCentrin4 knockdown (Figure 2 C, D).

We performed immunofluorescence microscopy of fixed TbCentrin4 RNAi cells and of TbCentrin4 and p197 double RNAi cells that had either been induced for the RNAi construct(s) for 65 h or not (Figure 2 C). To assess the presence of the TAC in TbCentrin4 RNAi zoid cells, we immuno-labelled the TAC component TAC102. We labelled the pBB and BB with the YL1/2 antibody (labelling tyrosinated tubulins at the BB and pBB, (Kilmartin et al., 1982)), while we stained DNA with DAPI. Upon induction of the RNAi construct we observe zoids (recognizable by the absence of nuclear DAPI signal). Such zoids consistently retained their kDNA signal at the posterior end of the cell. Furthermore, we observed that all cells remained TAC102 and YL1/2 positive, with both signals localizing similar to wild type cells.

TbCentrin4 p197 double RNAi cells on the other hand, were devoid of nuclear DNA and of kDNA, as expected. Furthermore, TAC102 signal was absent in TbCentrin4 p197 double RNAi zoids, while the YL1/2 signal was retained. The loss of TAC102 in these cells was expected, as TAC102 localization depends on the presence of p197 (Hoffmann et al., 2018). The BB and pBB, and thus YL1/2 signal, was not affected by TAC depletion, as previously reported (Hoffmann et al., 2018). These experiments indicate that the TAC remained intact after TbCentrin4 knockdown, while p197 knockdown led to the generation of kinetoplast-free, TAC-depleted zoid cells (tdzoids).

To further support an intact TAC morphology in zoid cells, we imaged by TEM chemically fixed and resin-embedded wild type cells and zoids (Figure 2 D). More than 40 TAC regions in either uninduced or induced TbCentrin4 RNAi cells were observed and no difference in TAC morphology was visible. Under both conditions, the area between the mitochondrial kDNA pocket and the (p)BB was devoid of ribosomes, confirming that the TAC was not perturbed by the zoid induction.

Morphology of the TAC area in *T. brucei* zoids

In many of our zoid cryo-electron tomograms, we could readily identify the TAC and surrounding structures such as the pBB, the BB, the flagellar pocket, the microtubule quartet and the mitochondrial kDNA pocket (Figure 3).

The overall organization we observed by cryo-ET matches our expectations from observations previously made by TEM of chemically fixed and resin-embedded wild type trypanosomes and isolated cytoskeletons (Ogbadoyi et al., 2003). Yet, for the first time, we observed the TAC region free of artifacts induced by chemical fixation and resin embedding. All cell membranes, including the

mitochondrial double membrane, had a smoother appearance than in chemically fixed and resin-embedded samples (compare Figure 2 D with Figure 3 A, B). The kDNA did not appear as dark as in fixed and stained preparations. This is partly due to the low contrast in the relatively thick area of the trypanosome, and partly due to the absence of heavy-metal staining.

Some TAC components could be visualized with an unpreceded level of detail. Between the proximal end of the BB and pBB, in the ribosome-free exclusion zone, we could clearly identify filaments, namely the EZFs (arrowheads in Figure 3 B, 3D-segmentation in Figure 3 C). The filaments are thin and wavy, and span the entire region between the BB and the OMM or the pBB and the OMM, respectively. In some cells we spotted dozens of filaments, while in other tomograms, we could only see a few. We believe the variability in filament count to result from low contrast due to fluctuations in cell thickness, ice quality and precision of tilt-series alignement, rather than from an absence of filaments. The EZFs were clearly visible in 30 % of our tomograms. To confirm that the filaments were indeed part of the TAC, we acquired over 30 tomograms of tdzoids. No filamentous structures between the (p)BB and the OMM could be found in any of them (Figure S 2). Instead, the area contained ribosomes, similar to the rest of the cytoplasm. This demonstrates that in the absence of p197, the exclusion zone and its filaments are not present.

Inside the mitochondrion, we did not observe any filamentous structures that would correspond to the ULFs, i.e. intramitochondrial components of the TAC. This is likely because the density of the ULFs is similar to the density of the mitochondrial matrix. We observed structures connecting the outer and inner mitochondrial membranes in the TAC area. These could be the well characterized OMM components of the TAC (pATOM36, TAC40, TAC42, TAC60) connecting to the IMM component p166 (Käser et al., 2016, 2017; Schnarwiler et al., 2014; Zhao et al., 2008). However, we observed similar structures in the area outside the TAC. The current resolution did not allow us to assess whether they differed. Nonetheless, the intermembrane distance is significantly smaller in the TAC area (8.2 ± 0.9 nm) than outside of it (9.9 ± 1.3 nm) (Figure 4 B). This suggests that the connection of TAC60 in the OMM to p166 in the IMM influences the mitochondrial intermembrane distance (Schimanski et al., 2022). This is in line with a different protein composition within the DMs, which was previously reported (Käser et al., 2017; Ogbadoyi et al., 2003; Schnarwiler et al., 2014).

We measured the minimal distance between the proximal face of the BB and the OMM, or the pBB and the OMM, respectively (Figure 4 C). pBBs were located on average 63 ± 81 nm away from the OMM, which is significantly less than the average distance of 145 ± 123 nm between BBs and the OMM. Furthermore, in 70 % of the cells, the pBB was closer to the OMM than the mature BB.

The exclusion zone filaments are highly flexible and allow a wide range of movement for the basal body and pro-basal body

As mentioned before, the orientation of the BBs towards each other and towards the mitochondrial membranes and kDNA was highly variable (examples depicted in Figure S 1). To quantify the extent of this observed diversity, and to enable us to spot potential preferred orientations, we measured the angles of the respective structures in relation to each other (Figure 5). With mean angles of 31.6 ± 31.3° and 35.4 ± 30.1°, the orientation of the BB and pBB in respect to the membranes was not

significantly different. The mean angle between the BB and pBB was 48.5 ± 39.8°. More striking than the mean angles however, was the wide spread of the data points. In Figure 5 B one can appreciate that the angle ranged from -78° to 84° for the BB, and from -52° to 87° for the pBB. Furthermore, the angle between BB and the pBB was equally as variable, with a range of 1° to 162° (Figure 5 D). Despite the wide spread, the most extreme values were quite rare overall. This is reflected by the standard deviations indicated in Figure 5 B and D. The histograms shown in Figure 5 C and E demonstrate that the vast majority of the observed angles between BB / pBB and the mitochondrial membranes were positive, comprised between 0° and 90°, and peaking in abundance around 45°. Small angles close to 0° were most abundant between the two BB types.

Structural analysis of individual exclusion zone filaments

Based on the available literature on the TAC and its components, we assumed p197 to be the protein we observe as the EZF in cryo-ET. In a recent study, p197 has been shown to span the entire exclusion zone (Aeschlimann et al., 2022). Using ultrastructure expansion microscopy, Aeschlimann and colleagues demonstrated that the N-terminus of p197 localizes to the DMs, while the C-terminus of the protein is localized to the BB and pBB. Between the N-terminal and C-terminal domains, p197 contains at least 26 nearly identical repeats of 175 - 182 amino acids each(Aeschlimann et al., 2022; Naguleswaran et al., 2021). p197 being the EZF is well in line with the observed absence of EZFs in cells depleted of p197 (tdzoids, Figure S 2).

The structure of p197 is not known. Given the flexibility of the EZFs, we did not attempt to perform subtomogram averaging of them. Instead, we followed an integrative approach, combining structural prediction and structural information that we could extract from our tomograms.

We measured the diameter of 100 EZFs from ten high contrast tomograms to be on average 4.57 ± 0.89 nm (Figure 6 B). We then measured the length of the EZFs in 22 tomograms. In each of these tomograms, we manually segmented five filaments and measured their length (Figure 6 C). The average length was 417.5 ± 89.2 nm, with considerable variation, ranging from 230 nm to 625 nm.

As the central repeat section of p197 makes up most of the protein, it likely corresponds to the filamentous structure of the EZFs observed in cryo-ET. We therefore modelled the repeat section with AlphaFold2 (Figure 6 D, (Jumper et al., 2021)). Due to hardware limitations, we could not model the full protein. Instead, we modelled a shorter sequence composed of the N-terminal domain, six repeats and the C-terminal domain (construct overview in Figure S 4). While the N- and C-terminal prediction was unstructured and had a low confidence score, a repetitive pattern of coiled coils is predicted for the central repeat section (Figure 6 D, Figure S 3). Each repetitive unit is composed of three antiparallel α-helices of 49, 51 and 49 amino acids, respectively, and an α-helical linker of 20 amino acids. This fold resembles the fold of the spectrin repeat (Liem, 2016). We therefore further refer to the p197 repetitive unit as spectrin-like unit.

To verify plausibility of the AlphaFold2 prediction, we compared the dimensions of the predicted p197 filaments to those of the filaments in our cryo-ET data. From a low-resolution map of the spectrin-like unit (calculated to a resolution of 1.5 nm) we measured the diameter at six positions along a spectrin-like unit and one position within the linker helix (Figure 6 E, top). Based on these

measurements we expect diameters ranging from 2.2 to 4.2 nm in the spectrin-like unit, while we expect values as small as 2 nm in the linker region. We then further calculated the theoretical length of the entire repeat section of p197 (assuming 26 repeats, as annotated in EATRO1125 (Naguleswaran et al., 2021)) to a value of 286 nm (Figure 6 E, bottom). The predicted length did not match most of our measurements in tomograms (Figure 6 C, E). While a few measurements are in the range of the predicted length, most of the filaments are considerably longer. Considering the variability of the (p)BB distance to the OMM (Figure 4 C), this matches our expectations. We therefore assume the structure predicted by AlphaFold2 to represent only one of several possible conformations of p197.

Also, the predicted diameter of individual p197 molecules did not entirely match the filament diameters measured in cryo-ET (Figure 4 B, B). While some measurements fall within the range of the predicted diameter of the spectrin-like unit, others suggest a diameter up to 1.5-fold the expected values. Such a discrepancy might result from delocalization effects of the contrast transfer function and the missing wedge effect. It could, on the other hand, reflect potential oligomerization of p197, or decoration of the protein with small proteins of unknown identity.

We conclude that p197 adopts the shape of a flexible filament consisting of an array of spectrin-like units. These repetitive units are flanked by the terminal domains that provide anchorage to the BB and downstream TAC components.

Discussion

The TAC is likely unique to the Kinetoplastea, and yet, some of its features show similarities to other systems and processes. Conceptually and functionally, the TAC closely resembles the mitotic kinetochore structure. This analogy has been put forward in a recent publication, based on the shared role in DNA segregation and the involvement of centrioles in the process (Amodeo et al., 2020). Centrioles are a common feature in many eukaryotic species, acting as microtubule organizing centers (MTOCs) and forming the base of flagella or cilia. The TAC in *T. brucei* serves as a striking example of divergent evolution, where a widespread structure has been repurposed for a unique function. At the same time, it is an example of convergent evolution, where two independent sets of proteins have evolved to perform the same function of separating replicated DNA.

To get a better understanding of how trypanosomes and other kinetoplastid species utilize their BBs to orchestrate segregation of a complex DNA network, it is crucial to observe the TAC structure in its native unperturbed environment. In this study we structurally characterized the EZFs and the DMs of the TAC, by applying cryo-ET to a genetically engineered cell line.

While thin sections produced by ultramicrotomy rarely simultaneously capture the BB, pBB and a middle section of the kDNA in a single cell, whole-cell tomography enabled us to observe these structures together. Tomographic imaging in intact zoid allowed us to avoid the detection bias created by manual search of the area of interest in fixed section TEM. When we image thin sections of chemically-fixed, resin-embedded cells, a cross-sectioned stained kDNA is very easy to spot, even at relatively low magnifications. We then zoom into those regions specifically, and search for a BB. If we see both structures, we are confident that, if there were a TAC, we would see it. In whole-cell

imaging we don't rely on this selective acquisition process. Instead, we can image the TAC region in any cell within the sample. Cryo-ET therefore allows for a more comprehensive analysis of samples, as opposed to the limited perspective provided by targeted search in 2D imaging. Our data shows that there is a high degree of orientational diversity within the TAC area, which is not typically captured by 2D imaging.

Qualitative observation of the TAC area in intact trypanosomes revealed the overall architecture of the complex (Figure 2 an Figure 3). We could clearly identify the EZFs. Quantitative analysis of the distance between the (p)BB and the DMs showed that the pBB often resides closer to the OMM, than the mature BB does (Figure 4 B). Furthermore, we could distinguish the DMs from the surrounding area of the mitochondrial membranes. Our analysis of the mitochondrial membranes demonstrated that the inter-membrane distance in the DM area was 17 % smaller compared to the surrounding area (Figure 4 C).

To investigate the structure of the EZF protein p197, we used an integrative approach combining quantitative analysis of cryo-electron tomograms, sequence analysis, AI-based structural predictions and information gathered from the literature (Figure 6). The experimental results obtained from the analysis of cryo-ET data provide insights into the diameter and length of the individual filaments (Figure 6 B, C). Structural predictions of the repeat section of p197 using AlphaFold2, suggest an organization in spectrin-like α-helical bundles (spectrin-like units, Figure 6 D). The spectrin-like units are predicted to be connected via an α-helical linker of sufficient length to enable the alignment of spectrin-like units to a filamentous stretch of coiled coils.

To align the AlphaFold2 prediction with the cryo-ET data, we extrapolated the six-repeat p197 predicted by AlphaFold2, to the full length of 26 repeats, and calculated the length of the repeat section to 286 nm. This number aligns well with the shortest filament lengths measured in cryo-ET (l_{min} = 230 nm, C). However, this theoretical length does not fit the length of most of the observed filaments (417.5 ± 89.2 nm, Figure 6 C). We therefore suggest that the structure predicted by AlphaFold2 only reflects the most stable state of the protein, while many filaments that we observed in cryo-ET likely assume different conformations in response to tensions arising from BB movement. One source of BB movement is imposed by the propelling movement of the flagellum (Figure 7 A). We assume it to cause a slight but constant tumbling of the BB.

Other sources of BB movements include the cell cycle dependent repositioning of the basal bodies in preparation of cell division. The first of these movements is the rotation of the new BB/pBB pair around the old BB during kinetoplast S-phase (Figure 7 B). This process displaces the new BB/pBB pair to a position posterior of the parental BB (Vaughan & Gull, 2016). Vaughan and colleagues showed that this rotation happens at late stages of pBB outgrowth, when the transition zone is fully formed and the new pBBs have been nucleated next to the old flagellum and the freshly matured BB (Vaughan & Gull, 2016). Our data show that the assembly of p197 at the new BB happens before these events. The filaments are fully assembled at the maturing BB before the nucleation of a fresh set of pBBs (Figure 3). This indicates that filaments are present at the time of BB rotation.

The second cell cycle dependent BB movement happens after the outgrowth of the new axoneme (Figure 7 C). At this stage, the kDNA has been fully replicated, and the two BB/pBB pairs separate (Schneider & Ochsenreiter, 2018). The connection between the BBs and the kDNA (provided by the TAC) allows for segregation of the kDNA along with BB separation (Ogbadoyi et al., 2003; Schneider & Ochsenreiter, 2018).

Collectively, cell motility, BB rotation and BB separation all require p197 to be sufficiently elastic to resist variable levels of mechanical force throughout the cell cycle. Our measurements of the distance and angular position of the BBs relative to the outer mitochondrial membrane clearly demonstrate that p197 indeed provides the flexibility suggested by its function (Figure 4 and Figure 5). The distance of the BB to the OMMs was highly variable, which supports our claim of a need for flexibility of the TAC (Figure 4). The observation of the angular variability between the (p)BB and the OMM further demonstrates the extend of flexibility p197 provides (Figure 5).

We hypothesize that under tension, individual spectrin-like units of p197 unfold to a single α-helix (Figure 7 D). The number of unfolded spectrin-like units should depend on the force applied to the individual filament. When all 26 units are unfolded, p197 reaches a maximum length of 690 nm. The predicted range of 286 nm to 690 nm aligns well with our observations in cryo-ET (230 – 625 nm, Figure 6 C). Previous research has demonstrated that temporary unfolding, or elasticity, plays a key role in the function of many spectrin-repeat containing proteins, such as the giant muscle protein titin (Djinovic-Carugo et al., 2002; Tskhovrebova et al., 1997). An engineered polymeric protein consisting of four identical spectrin domains was also shown to have elastic properties consistent with the unfolding pattern we predict for p197 (Lenne et al., 2000).

In case of p197, the mechanical force can vary not only over time, but also between the different filaments of a single BB at any given moment (Figure 7 E). We assume that both the releasable coiled coil of the spectrin-like unit and the α-helical linker contribute to the considerable variation in (p)BB positioning we observe in cryo-ET (Figure 4, Figure 5).

It was shown that deletion of the p197 spectrin-like units in *T. brucei* leads to loss of mitochondrial DNA, despite the proper localization of the protein and its ability to bind the BB and the OMM (Aeschlimann et al., 2022). The absence of spectrin-like units in the *T. cruzi* ortholog is consistent with the differences in cell cycle dynamics observed between the two parasites. (Elias et al., 2007; Vaughan & Gull, 2016). The absence of spectrin-like units in the *T. cruzi* ortholog of p197 further implies that a non-extendable, α-helical domain such as the one found in *T. cruzi* is sufficient to tolerate the effects of cell motility and BB separation – at least in *T. cruzi*. We therefore suggest that the most important role of the spectrin-like unit is the protein's structural response to the cell cycle dependent BB rotation in *T. brucei*.

To confirm the plausibility of the AlphaFold2 model, and to assess the oligomeric state of p197, we compared the diameter of the predicted spectrin-like unit with the diameter of the filaments as measured in cryo-ET. The range of 2 – 4.2 nm measured in the predicted structure is similar, but smaller than the range measured in the cryo-ET data (2.4 – 6.6 nm, B, Figure 6 A). While this discrepancy may reflect an artefact of the contrast transfer function and the missing wedge of the

tomographic data, it may also indicate p197 to oligomerize. Oligomerization of spectrin-repeat containing proteins is not unusual and has been shown for other spectrin-repeat proteins, such as spectrin or α-actinin (Djinovic-Carugo et al., 2002; Speichers et al., 1992). Alternatively, the protein may be decorated by other proteins that stabilize the filaments or assist correct folding and release of spectrin-like units.

In summary, our study describes the structure of the exclusion zone of the TAC. Using an integrative approach, we propose a model of the molecular structure of p197. It contradicts the notion of the TAC having a rather rigid structure suggested by earlier studies. More importantly however, the finding that p197 acts as a molecular spring provides an example of how a giant protein provides flexibility and stability for a dynamic cellular system.

Material and Methods

Trypanosoma brucei cell culture conditions

Procyclic form 29-13 asynchronous *T. brucei* cells were cultured in semi-defined medium-79 (SDM-79) supplemented with 10 % FCS, 15 µg/ml geneticin and 25 µg/ml hygromycin at 27° C (Wirtz et al., 1999). The cell line is part of the established collection of the Institute of Cell Biology, University of Bern, Bern, Switzerland.

From the 29-13 cell line, the two RNAi cell lines TbCentrin4 RNAi and TbCentrin4 p197 double RNAi were generated. Depending on the cell line, 5 µg/ml phleomycin and/or 10 µg/ml blasticidin was added to the media (see below). For RNAi induction, 1 µg/ml tetracycline was used.

Cloning of RNAi constructs

To clone the TbCentrin4 RNAi construct, we inserted base pairs 19-438 of the ORF (TREU927) into the pFC-4 vector. The sequence was obtained by PCR: FWD-primer: 5' – GTAAAAGCTTGGATCCGAACAGATCCGTGAAGCG – 3'; REV-primer: 5' GTAATCTAGACTCGAGCATCTGCATCATGACGCTC – 3'; template DNA: NYsm DNA isolate. Using the restriction sites (HindIII, BamHI, XbaI and XhoI) introduced by the primers, the target sequence was inserted twice (in opposite direction) to encode for a hairpin dsRNA. The pFC-4 plasmid contains blasticidin resistance. The p197 RNAi construct was previously described (Hoffmann et al., 2018). It encodes a hairpin dsRNA targeting the p197 ORF, and the phleomycin resistance gene.

Trypanosoma brucei transfections

To obtain the TbCentrin4 RNAi and TbCentrin4 p197 double RNAi cell lines, we transfected cells with the constructs described above. We integrated the constructs by homologous recombination. 10^8 29-13 PCF cells, or TbCentrin4 RNAi cells were used. The transfection mixtures consisted of 10 µg of linearized plasmid in 110 µl transfection buffer (90 mM sodium phosphate (pH 7.3), 5 mM KCl, 0.15 mM $CaCl_2$, 50 mM HEPES (pH 7.3))(Burkard et al., 2007). Cells were pelleted at 2'500 rcf for 8 min, mixed carefully with the transfection mixture and electroporated with the Amaxa Nucleofector (program X-014)(Schumann Burkard et al., 2011). After transfection, the cells were recovered in antibiotic free SDM-79 for 20 h. After the recovery, we added the respective antibiotics to select for

integration of the transfected constructs. To select for TbCentrin4 RNAi, we used 10 µg/ml blasticidin. For p197 RNAi, 5 µg/ml phleomycin were used.

Immunofluorescence analysis

10^6 cells were pelleted for 3 min at 1800 rcf. Cells were washed with 1 ml PBS, resuspended in 20 µl PBS and spread on a glass slide. After settling, cells were fixed for 4 min with 4 % paraformaldehyde in PBS. Following fixation, they were permeabilized for 5 min with 0.2 % Triton-X 100. The sample was then blocked with 4 % bovine serum albumin in PBS for 30 min. Cells were incubated with primary and secondary antibodies (diluted in blocking solution) for 45-60 min as follows: rat YL1/2 antibody detecting tyrosinated tubulin, which is found in the BB (Kilmartin et al., 1982)(a kind gift of Keith Gull) 1:10'000, monoclonal mouse anti-TAC102 antibody (Trikin et al., 2016) 1:5'000, Alexa Fluor® 488 goat anti-rat IgG (H+L)(Nanoprobes/FluoroNanogold) 1:1000, Alexa Fluor® 647 goat anti-mouse IgG (H+L)(Life technologies) 1:1000. After each antibody incubation step, cells were washed 3 x with 0.1 % Tween-20 (in PBS). A final wash with PBS was performed before mounting the cells in ProLong® Gold Antifade Mounting medium with DAPI (4',6-diamidine-2-phenylindole)(Invitrogen).

Fixed section transmission electron microscopy

Trypanosomes were grown as described above, harvested and centrifuged at 2500 rcf for 5 min. The pellets were fixed with 2.5 % glutaraldehyde in 0.15 M HEPES pH 7.41 at 4° C for at least 24 h. They were then washed with 0.15 M HEPES three times for 5 min, post-fixed with 1 % OsO4 in 0.1 M sodium cacodylate buffer at 4° C for 1 h, washed with 0.05 M maleate-NaOH buffer three times for 5 min. Subsequently the cells were dehydrated in 70, 80, and 96 % ethanol for 15 min each, at room temperature. Then the cells were immersed in 100 % ethanol three times for 10 min, in acetone two times for 10 min, and finally in acetone-epon (1:1) overnight, at room temperature. Cells were then embedded in pure epon and left to harden at 60° C for 5 days. Ultrathin sections (70–80 nm) were produced with an ultramicrotome UC6 (Leica Microsystems). The sections, mounted on 200 mesh copper grids, were stained with uranyless and lead citrate with an ultrostainer (Leica Microsystems). Sections were then examined with a transmission electron microscope (Tecnai Spirit, 80 kV) equipped with Olympus-SIS Veleta CCD camera.

Sample preparation for cryo-electron tomography of zoids

TbCentrin4 RNAi or TbCentrin4 p197 double RNAi PCF cells were RNAi induced for 65 h. The cells were then harvested by centrifugation at 2500 rcf, for 8 min. They were then resuspended in serum-free SDM-79 to a concentration of $2 \cdot 10^7$ cells/ml, and treated with a series of centrifugation steps: 26 rcf for 2 min, 68 rcf for 3 min, 210 rcf for 5 min. Then, the upper 35 % of the sample were collected for further centrifugation: 210 rcf for 3 min, 340 rcf for 5 min. We then collected the upper 55 % of this fraction, before centrifuging again, at 345 rcf for 3 min. At this point we collected the upper 60 % of the sample, and pelleted all cells remaining in this faction, by centrifugation at 1800 rcf for 7 min. The cells were washed in PBS, and then resuspended to a final concentration of $4 \cdot 10^7$ cells/ml. 10 nm gold beads (Aurion, OD520 = 2.0) were added 1:10 v:v. 3 µl of this sample were placed on a glow-discharged EM grid (lacey carbon films on Cu 200 mesh, Quantifoil Micro Tools), blotted from the back side for 3 s, and plunged into liquid ethane at a temperature of ≤ -170° C. The grids were stored in liquid nitrogen, until further use.

Tilt-series were acquired on Titan Krios transmission electron microscopes (Thermo Fisher Scientific) operating at 300 kV. The microscopes used were equipped with post-column energy filter, K2 (Gatan), K3 (Gatan) or Falcon4 (Thermo Fisher Scientific) direct electron detector, and in some cases, volta phase plate was used to enhance contrast at low defocus. Using SerialEM, tomograms were acquired as dose-symmetric tilt-series in 2° increments, ranging from -60° to +60°. A total electron dose of 120$e^-/Å^2$ was applied.

Sample preparation with focused ion beam milling

Cells were blotted on EM grids (R 2/1 holey carbon 200 films on Cu 200 mesh, Quantifoil Micro Tools). The grids were first glow-discharged and 4 µl of trypanosome wild-type culture (2-4 · 10^7 cells/ml) were placed on the grid. Using a Vitrobot Mark 4 (Thermo Fisher Scientific), cells were plunge frozen in a liquid ethane-propane mixture after blotting for 12 s at blotting force -4. Afterwards, grids were clipped into autogrid support rings with a cut-out that allows access to the ion beam at low angle (Thermo Fisher Scientific) and stored in liquid nitrogen until being used for FIB milling.

Cryo-FIB milling was performed as described previously (Schaffer et al., 2017) with an Aquilos 2 dual-beam FIB/ SEM instrument (Thermo Fisher Scientific). In the FIB/SEM chamber, grids were coated with a layer of organometallic platinum using a gas injection system to protect the sample surface. Micro-expansion joints (relief cuts) were milled to prevent lamella from bending (Wolff et al., 2019). A gallium ion beam was used for the milling. Owing to the small size of individual trypanosome cells, small clusters of cells were milled at a low angle (14-15°) to form short lamellae of 70-200 nm thickness. After milling, grids were transferred into a Titan Krios transmission electron microscope (Thermo Fisher Scientific), operating at 300 kV with a post-column energy filter (GIF Quantum LS, Gatan), and a direct detector camera (K2, Gatan). A total electron dose of 60-80$e^-/Å^2$ was distributed over a tilt range of -60° to +60°, with an increment of 2°. SerialEM was used for data collection.

Processing of cryo-electron tomograms

After acquisition, tilt-series of cryo-FIB milled trypanosomes were preprocessed using the TOMOMAN pipeline (v.0.6.9)(Wan, 2020) and custom MATLAB scripts. Raw frames of all tilt-series (including cryo-FIB milled trypanosomes as well as TbCentrin4 zoids and tdzoids) were then aligned using MotionCor2 (v1.3.2 or v.1.4.7)(Zheng et al., 2017). Then, each cryo-electron tomogram was reconstructed in IMOD (v4.12.0)(Mastronarde & Held, 2017), analysed visually, and tomograms were selected for further processing. This processing included deep learning based denoising using cryo-CARE (v0.1.1)(Buchholz et al., 2019) and in a few cases, manual segmentation of structures of interest, using IMOD. Tomograms from cryo-FIB milled trypanosomes were further processed with IsoNet (Liu et al., 2022), to compensate for missing wedge artifacts.

Distance measurements were conducted with the “measure” function of the IMOD drawing tools. Filament length was measured by placing contours on the relevant structures, and readout of all contour lengths of the respective IMOD model. Filament diameter was measured from manually selected stretches of well-resolved filaments. The local filament diameter was then measured from the intensity curve along a line drawn orthogonally to the filament direction. The effective diameter

was defined as the width of the intensity drop at half its depth. Intermembrane distance was measured using the FIJI macro "InteredgeDistance_v1.0.1_ImageJMacro.txt" found online (https://forum.image.sc/t/imagej-macro-to-measure-distance-between-two-lines-edges/42019). This macro takes two manually segmented lines as an input to return the distance between the two lines at 15 positions along them. The measured values correspond to the distance between centers of the respective membrane.

Angle measurements were performed using a custom-made python script. Upon entry of the coordinates of four points and a plane (defined by three points) in 3D space, the script calculates the normal vector of the plane, and the directional vectors of points one and two, and of points three and four, respectively. Based on the normal vector of the plane, and the directional vectors, it then further calculates the angle between each directional vector and the plane, as well as the angle between the two directional vectors. To apply this to our dataset, we defined the mitochondrial membranes in the TAC area as the plane, and the BB and pBB as directional vectors. We manually collected the respective points needed to define 3D orientation of the three objects of interest in the reconstructed tomograms.

BB / pBB distance to the mitochondrial membranes, angle measurements and filament length were measured on denoised tomograms acquired without volta phase plate, at defocus values ranging from -2 to -10 µm. EZF diameter was measured on non-filtered, unbinned (pixel size: 0.434 nm) tomograms acquired with volta phase plate, at defocus values of no more than -2.5 µm.

Circular statistics

Since angles are distributed on a circular scale, both angular extremes (close to 0° and close to 360°) are similar in direction, despite their numerical distance. Consequentially, statistical values must be calculated under consideration of this discrepancy from the linear scale (Berens, 2009; Schneiter et al., 2021). The circular mean and corresponding standard deviations where therefore calculated from the following equations:

$$\langle \vec{R} \rangle = \frac{1}{N} \sum_{q=1}^{N} \overrightarrow{R_q} = (\langle cos\gamma \rangle, \langle sin\gamma \rangle) \qquad (1)$$

$$\langle \gamma \rangle_c = arctan_2(\langle sin\gamma \rangle, \langle cos\gamma \rangle) \qquad (2)$$

$$S_c = \sqrt{-2ln(R)} \qquad (3)$$

$\langle \vec{R} \rangle$ hereby represents the mean resultant vector, which depends on the number N of angles, their respective values $\gamma_1 - \gamma_N$. Each angle γ_q was first transformed into its corresponding unit vector $\overrightarrow{R_q} = (cos\gamma_q, sin\gamma_q)$. The direction of $\langle \gamma \rangle_c$ of the mean resultant vector $\langle \vec{R} \rangle$ finally represents the mean direction.

The circular analogue to the standard deviation was derived from the length of the mean resultant vector $R = \left\| \langle \vec{R} \rangle \right\|$. It lies within the interval [0,1] and is described as S_c.

Calculations were performed using a python package for circular statistics available on GitHub: https://gist.github.com/kn1cht/89dc4f877a90ab3de4ddef84ad91124e

Modelling with AlphaFold2

For AlphaFold2 modelling, we used a truncated version of the amino acid sequence of 197 (EATRO1125, (Naguleswaran et al., 2021)) consisting of the N-terminal domain, six sequence repeats, one incomplete repeat (as this is also present in the annotated protein sequence), and the C-terminal domain (Figure S 4). Using the open-source code available on github.com AlphaFold2 was run on an in-house workstation. Monomeric p197 was run in AlphaFold2 multimer preset, predicting a total of five models. Model 4 was selected for further processing, based on highest LDDT scores in the repeat section (Figure S 3).

The theoretical filament diameter was determined based on a low-resolution map (1.5 nm) generated from the most N-terminal two units of the AlphaFold2 model (mapping performed in Chimera 1.16). Diameters of the filament cross-section were measured at six different positions along the coiled coil and one position within the linker (at each position, the largest and smallest diameter was measured).

Acknowledgments

This work was mainly funded by project grants to Torsten Ochsenreiter from Uniscientia and the Swiss National Science Foundation (grant number 179454) and by a project grant to Benoît Zuber from the Swiss National Science Foundation (grant number 179520). We acknowledge Diamond for access and support of the cryo-EM facilities at the UK national Bio-Imaging Centre (eBIC), proposals BI26915 and NT21004, funded by the Wellcome Trust, MRC and BBSRC. Equipment supported by the Microscopy Imaging Center (MIC) of the University of Bern, the eBIC of the Diamond Light Source, the BioEM facility of the University of Basel and ScopeM of the ETH Zürich was used during this study. Contributions from Takashi Ishikawa were funded by the grant number 310030_192644 of the Swiss National Science Foundation.

References

Aeschlimann, S., Kalichava, A., Schimanski, B., Berger, B. M., Jetishi, C., Stettler, P., Ochsenreiter, T., & Schneider, A. (2022). Single p197 molecules of the mitochondrial genome segregation system of Trypanosoma brucei determine the distance between basal body and outer membrane. *Proceedings of the National Academy of Sciences*, *119*(40). https://doi.org/10.1073/pnas.2204294119

Amodeo, S., Bregy, I., & Ochsenreiter, T. (2022). Mitochondrial genome maintenance - the kinetoplast story. *FEMS Microbiology Reviews*. https://doi.org/10.1093/FEMSRE/FUAC047

Amodeo, S., Hoffmann, A., Fradera-Sola, A., Bregy, I., Baudouin, H., Haenni, B., Zuber, B., Butter, F., & Ochsenreiter, T. (2020). Characterization of two novel proteins involved in mitochondrial DNA anchoring. *BioRxiv*, 2020.07.22.215871. https://doi.org/10.1101/2020.07.22.215871

Berens, P. (2009). CircStat: A MATLAB Toolbox for Circular Statistics. *Journal of Statistical Software*, *31*(10), 1–21. https://doi.org/10.18637/JSS.V031.I10

Braymer, J. J., & Lill, R. (2017). Iron–sulfur cluster biogenesis and trafficking in mitochondria. In *Journal of Biological Chemistry* (Vol. 292, Issue 31, pp. 12754–12763). American Society for Biochemistry and Molecular Biology Inc. https://doi.org/10.1074/jbc.R117.787101

Buchholz, T.-O., Jordan, M., Pigino, G., & Jug, F. (2019). Cryo-CARE: Content-Aware Image Restoration for Cryo-Transmission Electron Microscopy Data. *2019 IEEE 16th International Symposium on Biomedical Imaging (ISBI 2019)*, 502–506. https://doi.org/10.1109/ISBI.2019.8759519

Burkard, G., Fragoso, C. M., & Roditi, I. (2007). Highly efficient stable transformation of bloodstream forms of Trypanosoma brucei. *Molecular and Biochemical Parasitology*, *153*(2), 220–223. https://doi.org/10.1016/j.molbiopara.2007.02.008

Chen, J., Rauch, C. A., White, J. H., Englund, P. T., & Cozzarelli, N. R. (1995). The topology of the kinetoplast DNA network. *Cell*, *80*(1), 61–69. https://doi.org/10.1016/0092-8674(95)90451-4

Djinovic-Carugo, K., Gautel, M., Ylänne, J., & Young, P. (2002). The spectrin repeat: A structural platform for cytoskeletal protein assemblies. *FEBS Letters*, *513*(1), 119–123. https://doi.org/10.1016/S0014-5793(01)03304-X

Elias, M. C., da Cunha, J. P. C., de Faria, F. P., Mortara, R. A., Freymüller, E., & Schenkman, S. (2007). Morphological Events during the Trypanosoma cruzi Cell Cycle. *Protist*, *158*(2), 147–157. https://doi.org/10.1016/J.PROTIS.2006.10.002

Friedman, J. R., & Nunnari, J. (2014). Mitochondrial form and function. *Nature*, *505*(7483), 335–343. https://doi.org/10.1038/nature12985

Gheiratmand, L., Brasseur, A., Zhou, Q., & He, C. Y. (2013). Biochemical characterization of the bi-lobe reveals a continuous structural network linking the bi-lobe to other single-copied organelles in Trypanosoma brucei. *The Journal of Biological Chemistry*, *288*(5), 3489–3499. https://doi.org/10.1074/jbc.M112.417428

595 Hajduk, S., & Ochsenreiter, T. (2010). RNA editing in kinetoplastids. *RNA Biology*, *7*(2), 229–236.
596 https://doi.org/10.4161/rna.7.2.11393

597 Hoffmann, A., Käser, S., Jakob, M., Amodeo, S., Peitsch, C., Týč, J., Vaughan, S., Zuber, B., Schneider,
598 A., & Ochsenreiter, T. (2018). Molecular model of the mitochondrial genome segregation
599 machinery in Trypanosoma brucei. *Proceedings of the National Academy of Sciences of the*
600 *United States of America*, *115*(8), E1809–E1818. https://doi.org/10.1073/pnas.1716582115

601 Hong, M., & Simpson, L. (2003). Genomic organization of Trypanosoma brucei kinetoplast DNA
602 minicircles. *Protist*, *154*(2), 265–279. https://doi.org/10.1078/143446103322166554

603 Jakob, M., Hoffmann, A., Amodeo, S., Peitsch, C., Zuber, B., & Ochsenreiter, T. (2016). Mitochondrial
604 growth during the cell cycle of Trypanosoma brucei bloodstream forms. *Scientific Reports*, *6*.
605 https://doi.org/10.1038/srep36565

606 Jensen, R. E., & Englund, P. T. (2012). Network news: the replication of kinetoplast DNA. *Annual*
607 *Review of Microbiology*, *66*, 473–491. https://doi.org/10.1146/annurev-micro-092611-150057

608 Jumper, J., Evans, R., Pritzel, A., Green, T., Figurnov, M., Ronneberger, O., Tunyasuvunakool, K.,
609 Bates, R., Žídek, A., Potapenko, A., Bridgland, A., Meyer, C., Kohl, S. A. A., Ballard, A. J., Cowie,
610 A., Romera-Paredes, B., Nikolov, S., Jain, R., Adler, J., … Hassabis, D. (2021). Highly accurate
611 protein structure prediction with AlphaFold. *Nature*, *596*(7873), 583–589.
612 https://doi.org/10.1038/s41586-021-03819-2

613 Käser, S., Oeljeklaus, S., Týč, J., Vaughan, S., Warscheid, B., & Schneider, A. (2016). Outer membrane
614 protein functions as integrator of protein import and DNA inheritance in mitochondria.
615 *Proceedings of the National Academy of Sciences*, *113*(31), E4467–E4475.
616 https://doi.org/10.1073/pnas.1605497113

617 Käser, S., Willemin, M., Schnarwiler, F., Schimanski, B., Poveda-Huertes, D., Oeljeklaus, S., Haenni, B.,
618 Zuber, B., Warscheid, B., Meisinger, C., & Schneider, A. (2017). Biogenesis of the mitochondrial
619 DNA inheritance machinery in the mitochondrial outer membrane of Trypanosoma brucei. *PLoS*
620 *Pathogens*, *13*(12), e1006808. https://doi.org/10.1371/journal.ppat.1006808

621 Kilmartin, J. v, Wright, B., & Milstein, C. (1982). Rat monoclonal antitubulin antibodies derived by
622 using a new nonsecreting rat cell line. *The Journal of Cell Biology*, *93*(3), 576–582.
623 https://doi.org/10.1083/jcb.93.3.576

624 Lenne, P. F., Raae, A. J., Altmann, S. M., Saraste, M., & Hörber, J. K. H. (2000). States and transitions
625 during forced unfolding of a single spectrin repeat. *FEBS Letters*, *476*(3), 124–128.
626 https://doi.org/10.1016/S0014-5793(00)01704-X

627 Liem, R. K. H. (2016). Cytoskeletal Integrators: The Spectrin Superfamily. *Cold Spring Harbor*
628 *Perspectives in Biology*, *8*(10). https://doi.org/10.1101/CSHPERSPECT.A018259

629 Liu, Y. T., Zhang, H., Wang, H., Tao, C. L., Bi, G. Q., & Zhou, Z. H. (2022). Isotropic reconstruction for
630 electron tomography with deep learning. *Nature Communications*, *13*(1).
631 https://doi.org/10.1038/S41467-022-33957-8

632 Marko, M., Hsieh, C., Schalek, R., Frank, J., & Mannella, C. (2007). Focused-ion-beam thinning of
633 frozen-hydrated biological specimens for cryo-electron microscopy. *Nature Methods 2007 4:3*,
634 *4*(3), 215–217. https://doi.org/10.1038/nmeth1014

635 Mastronarde, D. N., & Held, S. R. (2017). Automated Tilt Series Alignment and Tomographic
636 Reconstruction in IMOD. *Journal of Structural Biology*, *197*(2), 102.
637 https://doi.org/10.1016/J.JSB.2016.07.011

638 Naguleswaran, A., Fernandes, P., Bevkal, S., Rehmann, R., Nicholson, P., & Roditi, I. (2021).
639 Developmental changes and metabolic reprogramming during establishment of infection and
640 progression of Trypanosoma brucei brucei through its insect host. *PLoS Neglected Tropical*
641 *Diseases*, *15*(9). https://doi.org/10.1371/JOURNAL.PNTD.0009504

642 Ochsenreiter, T., Cipriano, M., & Hajduk, S. L. (2007). KISS: The kinetoplastid RNA editing sequence
643 search tool. *RNA*, *13*(1), 1–4. https://doi.org/10.1261/rna.232907

644 Ogbadoyi, E. O., Robinson, D. R., & Gull, K. (2003). A high-order trans-membrane structural linkage is
645 responsible for mitochondrial genome positioning and segregation by flagellar basal bodies in
646 trypanosomes. *Molecular Biology of the Cell*, *14*(5), 1769–1779.
647 https://doi.org/10.1091/mbc.e02-08-0525

648 Povelones, M. L. (2014). Beyond replication: division and segregation of mitochondrial DNA in
649 kinetoplastids. *Molecular and Biochemical Parasitology*, *196*(1), 53–60.
650 https://doi.org/10.1016/j.molbiopara.2014.03.008

651 Robinson, D. R., Sherwin, T., Ploubidou, A., Byard, E. H., & Gull, K. (1995). Microtubule polarity and
652 dynamics in the control of organelle positioning, segregation, and cytokinesis in the
653 trypanosome cell cycle. *The Journal of Cell Biology*, *128*(6), 1163.
654 https://doi.org/10.1083/JCB.128.6.1163

655 Schaffer, M., Mahamid, J., Engel, B. D., Laugks, T., Baumeister, W., & Plitzko, J. M. (2017). Optimized
656 cryo-focused ion beam sample preparation aimed at in situ structural studies of membrane
657 proteins. *Journal of Structural Biology*, *197*(2), 73–82.
658 https://doi.org/10.1016/J.JSB.2016.07.010

659 Schimanski, B., Aeschlimann, S., Stettler, P., Käser, S., Gala, M. G. F., Bender, J., Warscheid, B., Vögtle,
660 F. N., & Schneider, A. (2022). p166 links membrane and intramitochondrial modules of the
661 trypanosomal tripartite attachment complex. *PLoS Pathogens*, *18*(6).
662 https://doi.org/10.1371/JOURNAL.PPAT.1010207

663 Schnarwiler, F., Niemann, M., Doiron, N., Harsman, A., Kaser, S., Mani, J., Chanfon, A., Dewar, C. E.,
664 Oeljeklaus, S., Jackson, C. B., Pusnik, M., Schmidt, O., Meisinger, C., Hiller, S., Warscheid, B.,

Schnaufer, A. C., Ochsenreiter, T., & Schneider, A. (2014). Trypanosomal TAC40 constitutes a novel subclass of mitochondrial B-barrel proteins specialized in mitochondrial genome inheritance. *Proceedings of the National Academy of Sciences*, *111*(21), 7624–7629. https://doi.org/10.1073/pnas.1404854111

Schneider, A., & Ochsenreiter, T. (2018). Failure is not an option – mitochondrial genome segregation in trypanosomes. *Journal of Cell Science*, *131*(18), jcs221820. https://doi.org/10.1242/jcs.221820

Schneiter, M., Halm, S., Odriozola, A., Mogel, H., Rička, J., Stoffel, M. H., Zuber, B., Frenz, M., & Tschanz, S. A. (2021). Multi-scale alignment of respiratory cilia and its relation to mucociliary function. *Journal of Structural Biology*, *213*(1). https://doi.org/10.1016/J.JSB.2020.107680

Schumann Burkard, G., Jutzi, P., & Roditi, I. (2011). Genome-wide RNAi screens in bloodstream form trypanosomes identify drug transporters. *Molecular and Biochemical Parasitology*, *175*(1), 91–94. https://doi.org/10.1016/j.molbiopara.2010.09.002

Shi, J., Franklin, J. B., Yelinek, J. T., Ebersberger, I., Warren, G., & He, C. Y. (2008). Centrin4 coordinates cell and nuclear division in T. brucei. *Journal of Cell Science*, *121*(Pt 18), 3062–3070. https://doi.org/10.1242/jcs.030643

Speichers, D. W., Weglarz, L., & Desilva, T. M. (1992). Properties of Human Red Cell Spectrin Heterodimer (Side-to-Side) Assembly and Identification of an Essential Nucleation Site. *Journal of Biological Chemistry*, *267*(21), 14775–14782. https://doi.org/10.1016/S0021-9258(18)42107-2

Sun, S. Y., Kaelber, J. T., Chen, M., Dong, X., Nematbakhsh, Y., Shi, J., Dougherty, M., Lim, C. T., Schmid, M. F., Chiu, W., & He, C. Y. (2018). Flagellum couples cell shape to motility in Trypanosoma brucei. *Proceedings of the National Academy of Sciences of the United States of America*, *115*(26), E5916–E5925. https://doi.org/10.1073/pnas.1722618115

Trager, W. (1965). The Kinetoplast and Differentiation in Certain Parasitic Protozoa. *The American Naturalist*, *99*(907), 255–266. https://doi.org/10.1086/282371

Trikin, R., Doiron, N., Hoffmann, A., Haenni, B., Jakob, M., Schnaufer, A., Schimanski, B., Zuber, B., & Ochsenreiter, T. (2016). TAC102 Is a Novel Component of the Mitochondrial Genome Segregation Machinery in Trypanosomes. *PLOS Pathogens*, *12*(5), e1005586. https://doi.org/10.1371/journal.ppat.1005586

Tskhovrebova, L., Trinick, J., Sleep, J. A., & Simmons, R. M. (1997). Elasticity and unfolding of single molecules of the giant muscle protein titin. *Letters to Nature*, *387*(15), 308–312.

Tyler, K. M., Matthews, K. R., & Gull, K. (2001). Anisomorphic cell division by African trypanosomes. *Protist*, *152*(4), 367–378. https://doi.org/10.1078/1434-4610-00074

Vaughan, S., & Gull, K. (2016). Basal body structure and cell cycle-dependent biogenesis in Trypanosoma brucei. *Cilia*, *5*(1), 5. https://doi.org/10.1186/s13630-016-0023-7

Wan, W. (2020). *TOMOMAN* (No. 0804020). Zenodo. https://doi.org/10.5281/zenodo.4110737

Wirtz, E., Leal, S., Ochatt, C., & Cross, G. A. (1999). A tightly regulated inducible expression system for conditional gene knock-outs and dominant-negative genetics in Trypanosoma brucei. *Molecular and Biochemical Parasitology*, *99*(1), 89–101. https://doi.org/10.1016/s0166-6851(99)00002-x

Wolff, G., Limpens, R. W. A. L., Zheng, S., Snijder, E. J., Agard, D. A., Koster, A. J., & Bárcena, M. (2019). Mind the gap: Micro-expansion joints drastically decrease the bending of FIB-milled cryo-lamellae. *Journal of Structural Biology*, *208*(3). https://doi.org/10.1016/J.JSB.2019.09.006

Zhao, Z., Lindsay, M. E., Roy Chowdhury, A., Robinson, D. R., & Englund, P. T. (2008). p166, a link between the trypanosome mitochondrial DNA and flagellum, mediates genome segregation. *The EMBO Journal*, *27*(1), 143–154. https://doi.org/10.1038/sj.emboj.7601956

Zheng, S. Q., Palovcak, E., Armache, J. P., Verba, K. A., Cheng, Y., & Agard, D. A. (2017). MotionCor2 - anisotropic correction of beam-induced motion for improved cryo-electron microscopy. *Nature Methods*, *14*(4), 331. https://doi.org/10.1038/NMETH.4193

Figures

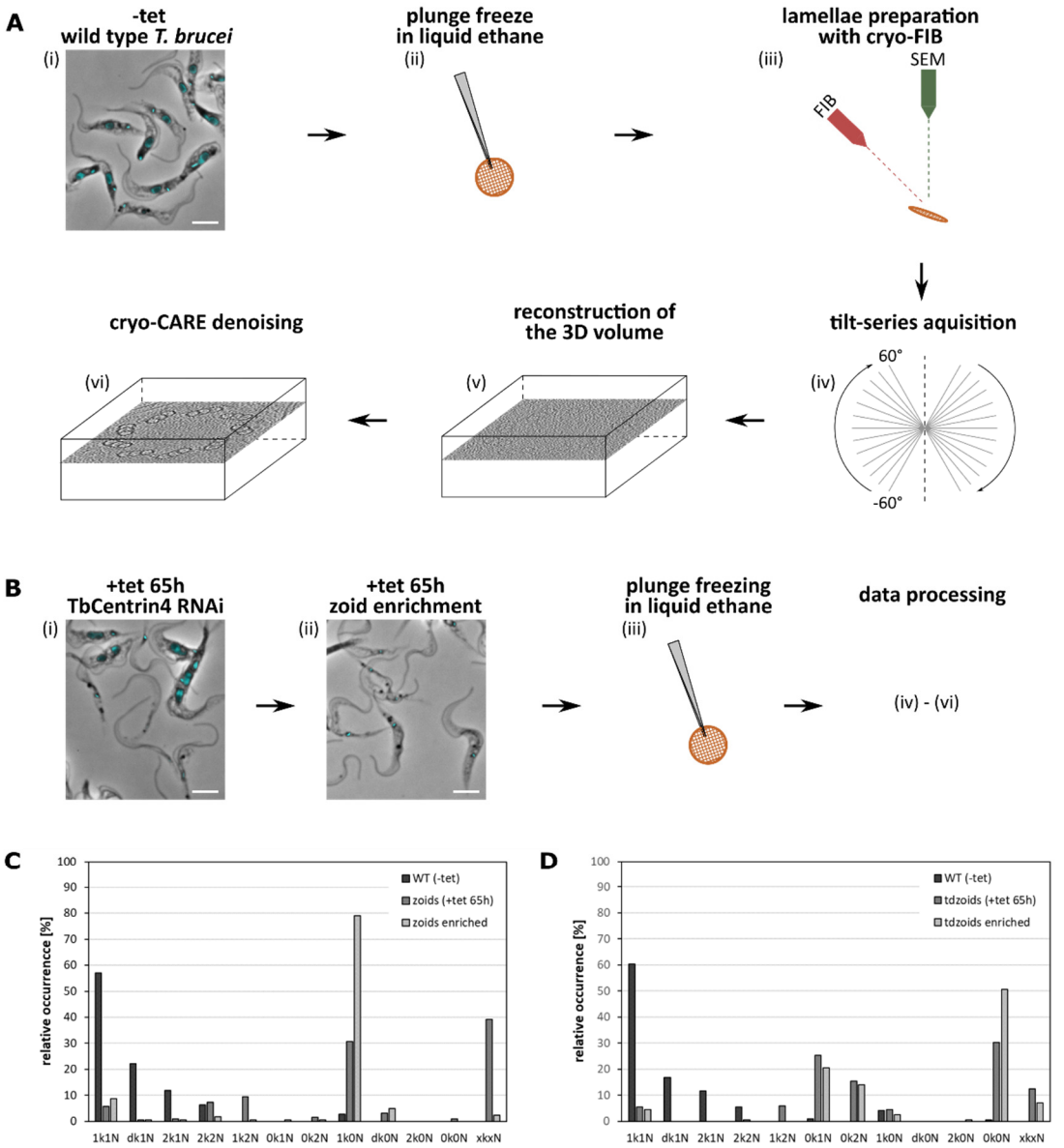

Figure 1: Overview of the cryo-ET workflow.

A) Schematic overview of the workflow for cryo-FIB milling, cryo-ET and subsequent data processing. (i) Wild type procyclic form trypanosomes are (ii) mounted onto carbon coated copper grids and plunge frozen in liquid ethane. From this point on, the samples are kept at liquid nitrogen temperature at all times. The samples are transferred to an Aquilos 2 scanning electron microscope equipped with a focused ion beam source (FIB) and (iii) lamellae of about 70-200 nm thickness are randomly milled through the trypanosomes. The samples are then transferred to the Titan Krios transmission electron microscope (TEM), where tomographic datasets are collected as (iv) a tilt-series of low dose micrographs. The tilt-series is then (v) preprocessed and reconstructed using TOMOMAN, MotionCor2 and IMOD, and (vi) denoised with cryo-CARE (Buchholz et al., 2019; Mastronarde & Held, 2017; Wan, 2020; Zheng et al., 2017). The micrograph in (i) shows an overlay of phase contrast with the DNA stain DAPI; scale bar: 5µm. B) Schematic overview of the experimental workflow for cryo-ET of zoids and tdzoids. *T. brucei* cells carrying the TbCentrin4 RNAi (and p197

RNAi) contruct, are (i) induced for RNAi expression for 65 h hours. The resulting population of trypanosomes (containing about 30 % of zoids) is then harvested, and (ii) enriched for zoids. The zoid fraction is then (iii) transferred to carbon coated copper grids and plunge frozen in liquid ethane. Data acquisition and processing (steps (iv) to (vi)) are identical to the description in A, except for TOMOMAN preprocessing, which was skipped in this case. Micrographs in (i) and (ii) show an overlay of phase contrast with the DNA stain DAPI; scale bar: 5µm. C) Karyotype distributions of wild type *T. brucei* (black), TbCentrin4 RNAi cells induced for 65 h (zoids, dark grey) and TbCentrin4 RNAi cells after induction (65 h) and centrifugal enrichment of zoids (zoids enriched, light grey). n ≥ 150. D) Karyotype distributions of wild type *T. brucei* (black), TbCentrin4 p197 double RNAi cells induced for 65 h (tdzoids, dark grey) and TbCentrin4 p197 double RNAi cells after induction (65 h) and centrifugal enrichment of tdzoids (tdzoids enriched, light grey). n ≥ 150.

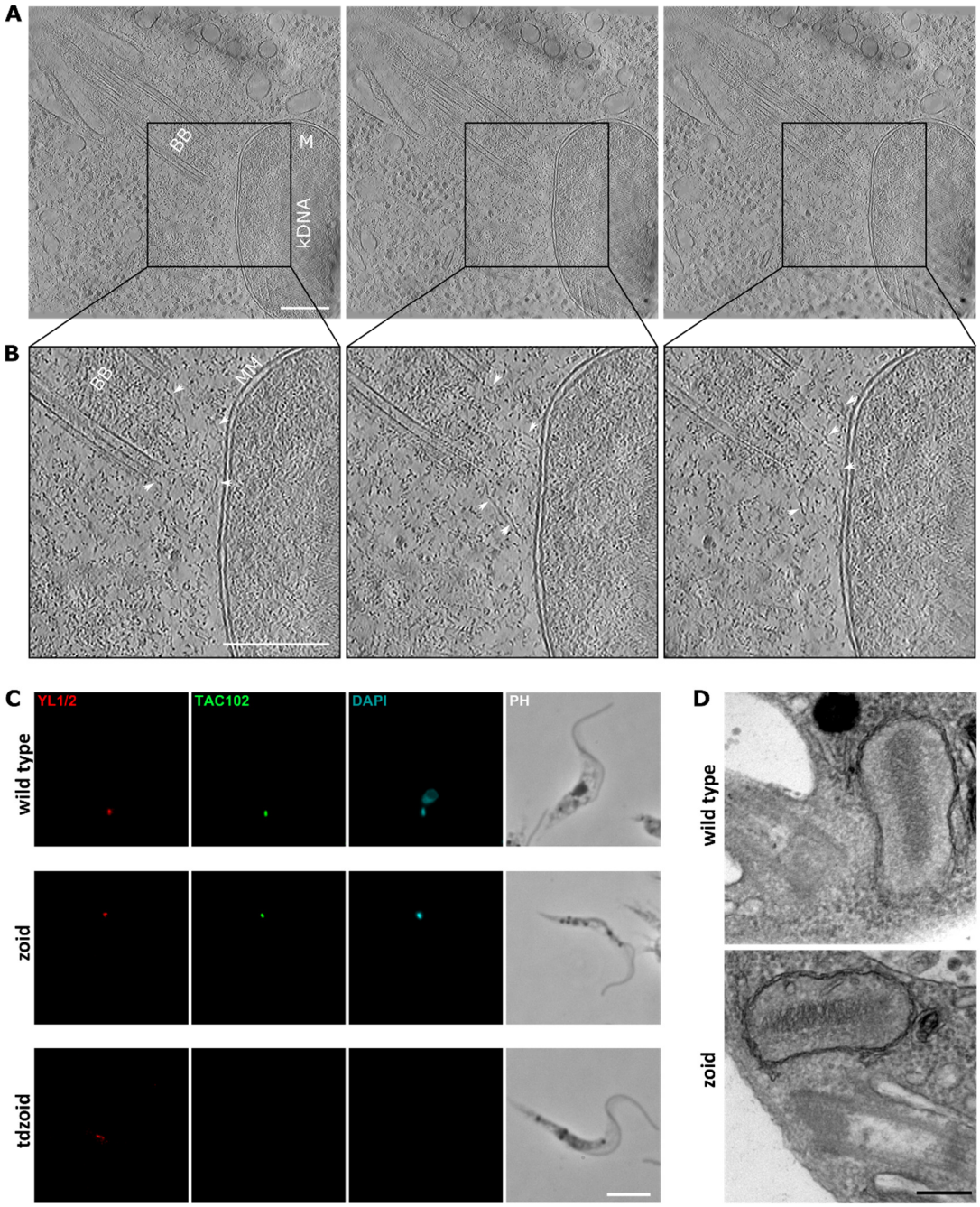

Figure 2: cryo-FIB milling of wild type *T. brucei* and zoid generation by TbCentrin4 RNAi are two alternative approaches for TAC imaging by cryo-ET.

A) Micrographs showing three tomographic z-slices through the TAC region of a wild type *T. brucei* cell. Basal body (BB), mitochondrial kDNA pocket (M) and kDNA are labelled in the images on the left. Scale bar: 200 nm. Full tomogram shown in Movie S 1. B) Magnified images of the exclusion zone. Filamentous structures protrude from the proximal end of the BB towards the mitochondrial membranes (MM). Some well-resolved filaments are marked with arrowheads. Scale bar: 100 nm. C) Immunofluorescence analysis of wild type trypanosomes (top row), zoids (middle) and tdzoids (bottom). The cells were stained with the BB marker YL1/2, that stains for tyrosinated tubulins at the BB, with monoclonal anti-TAC102 antibody and with the DNA stain DAPI. Scale bar: 5 µm. D) TEM

analysis of the TAC region in chemically fixed, resin-embedded wild type trypanosomes (top) and zoids (bottom). Scale bar: 250 nm.

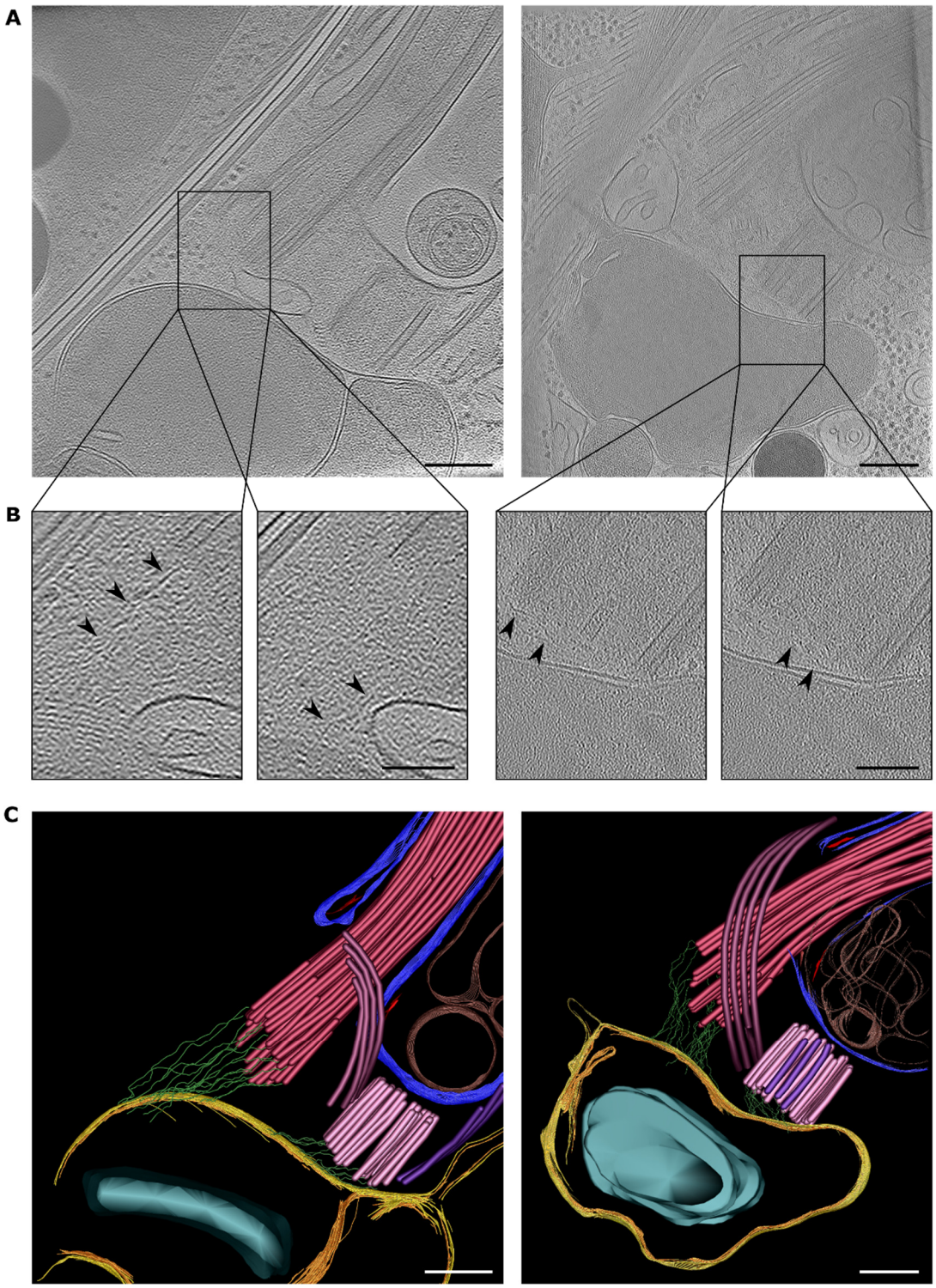

752 Figure 3: Phenotypical overview and segmentation of the TAC area of zoid *T. brucei* as
753 observed in situ by cryo-ET.
754 A) Section (maximum intensity projection of 20 slices) through two typical cryo-electron tomograms.
755 Scale bars: 200 nm. Full tomograms shown in Movies S 2 and S 3. B) zoom-in into the exclusion zone,
756 highlighting individual EZFs (maximum intensity projection of 10 slices; arrowheads pointing at the
757 most well-resolved filament in the respective image). Scale bars: 100 nm. C) Model of the TAC area
758 based on segmentations of the tomograms shown in A. BB and flagellum (magenta), pBB (pink),
759 microtubule quartet of the mature BB (purple), growing microtubule quartet of the pBB (violet),

760 flagellar pocket (blue), flagellar pocket vesicles (brown), collarette (red), exclusion zone filaments of
761 the TAC (green), outer mitochondrial membrane (yellow), inner mitochondrial membrane (orange)
762 and kDNA (cyan) have been segmented in cryo-CARE (Buchholz et al., 2019) denoised tomograms.
763 Scale bars: 200 nm. Animations in Movies S 4 and S 5.

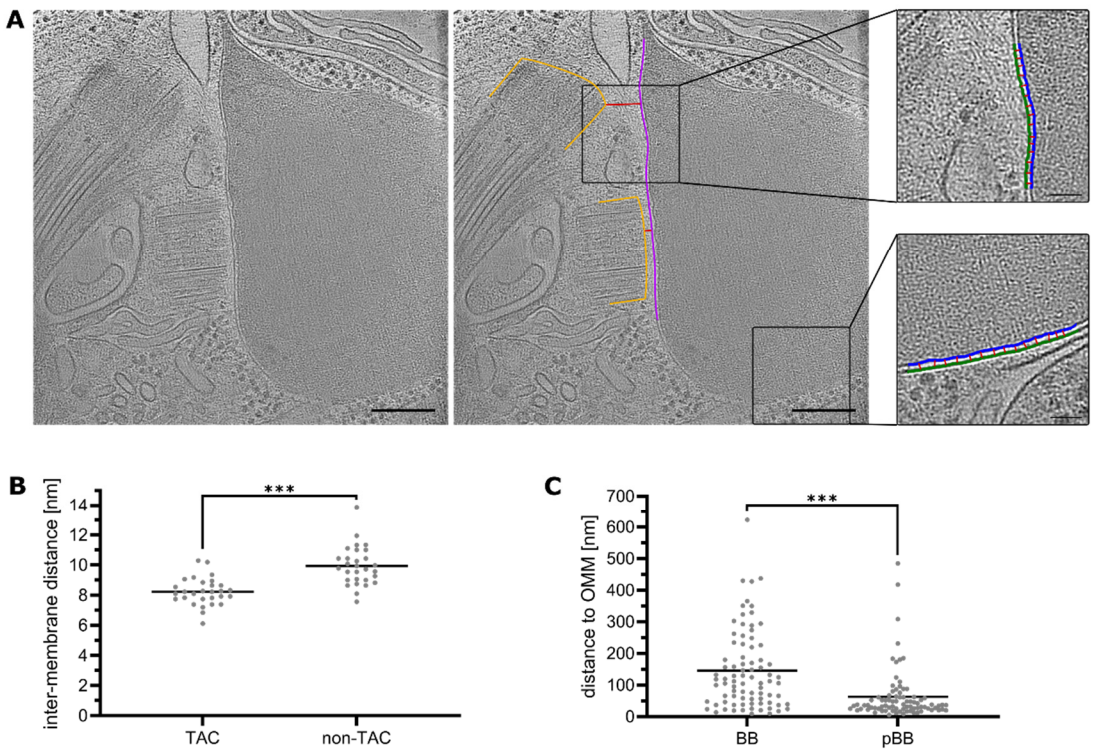

Figure 4: Dimensions of the exclusion zone and the differentiated membranes as observed in cryo-ET.

A) Overview of the measured dimensions in a representative tomogram. (left) single z-slice of a representative tomogram of the TAC area of a *T. brucei* zoid cell; (middle) demonstration of the measurement strategy applied for (C), with the orange line outlining the proximal part of the BB/pBB, pink following the outer mitochondrial membrane (OMM) and red showing the measured distances for BB and pBB distance to the OMM; (right) zoom-in at two membrane patches, one within the TAC area (top) and one outside the TAC area (bottom), blue and green showing inner and outer mitochondrial membrane (IMM and OMM) , red indicating the measured distances (center of the OMM to center of the IMM). Scale bars: 200 nm / 50 nm. Full tomogram shown in Movie S 6. B) Depiction of the results from measurements of the inter-membrane distance of the mitochondrial membranes in the TAC area versus the membrane area outside of the TAC (non-TAC) (measurements from 29 cells, with 15 averaged measurements per membrane patch). Asterisks (*** ≙ $p \leq 0.001$) indicate significance of the difference in intermembrane distance. p-value (two-sided t-test) = $5 \cdot 10^{-10}$. C) Collective display of distance measurements obtained from 82 cells. Asterisks (*** ≙ $p \leq 0.001$) indicate that the pBB is positioned significantly closer to the OMM than the mature BB is. p-value (two-sided t-test) = $1.4 \cdot 10^{-6}$.

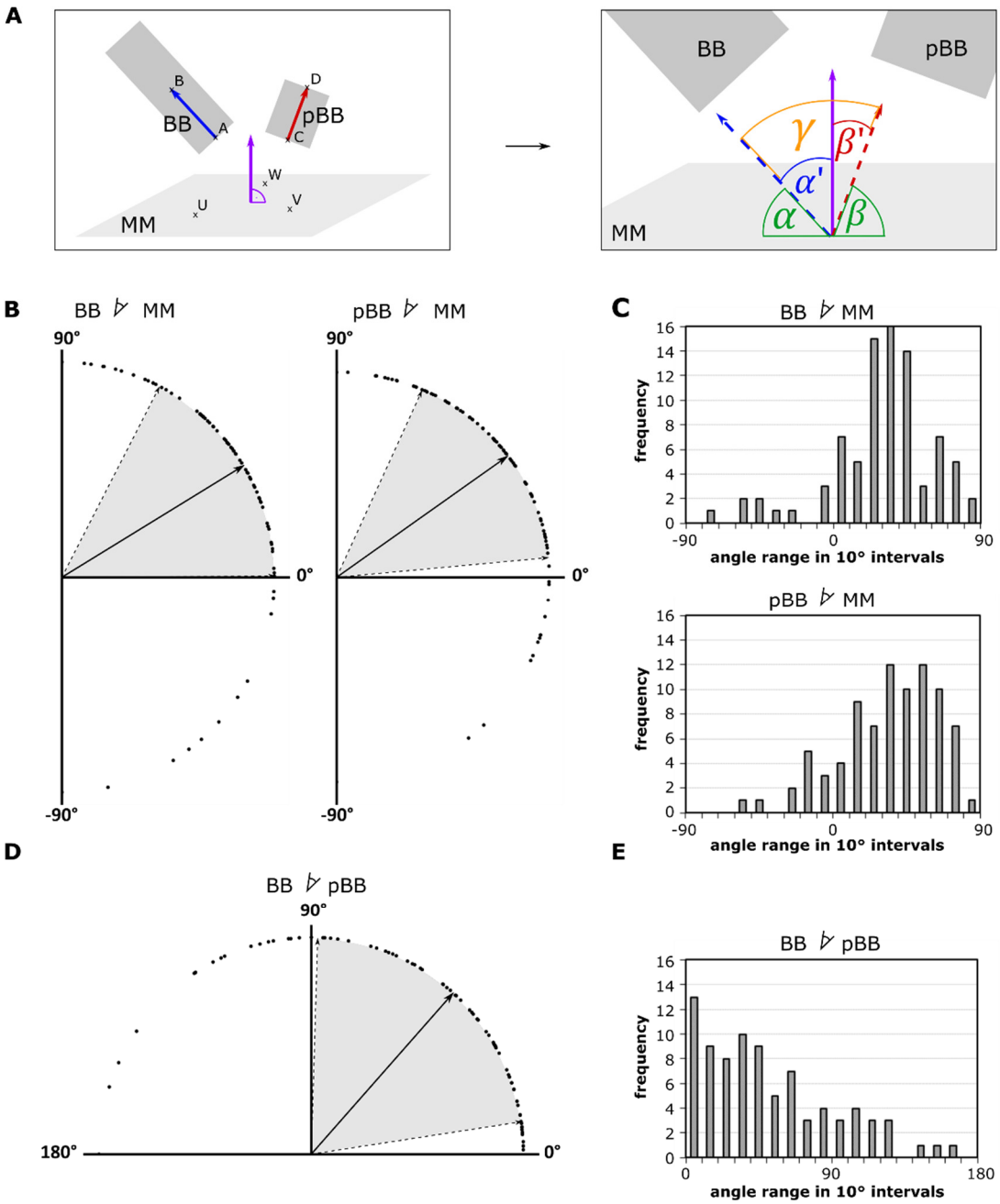

781 Figure 5: The exclusion zone filaments are highly flexible and allow a wide range of
782 movement for the basal body and pro-basal body.

783 A) In 3D space we selected three points on the outer mitochondrial membranes (MM; points U, V,
784 W), and two points along the axis of the BB (blue, points A, B) or pBB (red, points C, D). We calculated
785 the angles between the resulting vectors $\overrightarrow{AB}$ and $\overrightarrow{CD}$ for the BB (blue, α') or pBB (red, β') respectively,
786 and the normal vector on the plane built by U, V and W (purple). From these angles, we deduced the
787 angles between vectors $\overrightarrow{AB}$ (green, α) or $\overrightarrow{CD}$ (green, β) and the plane itself. To obtain the vector
788 between BB and pBB, we calculated the angle between $\overrightarrow{AB}$ and $\overrightarrow{CD}$ (orange, γ). B) Visualization of the
789 angles measured between the BB and the MM (left), or the pBB and the MM (right). The membrane
790 plane was selected to be in the area of the TAC, irrespective of the position of any other parts of the
791 MM. The X-axis of each graph represents an angle of 0° between the two structures in question,
792 while points hitting the Y-axis are at a 90°/-90° angle to the MM. The mean angles of 31.6° (BB-MM)

or 35.4° (pBB-MM) as well as the standard deviations of 31.3° (BB-MM) or 30.1° (pBB-MM) are marked with arrows. The respective standard directional range is shown in grey. C) Histograms illustrating the distribution of the data points shown in B (bin size = 10°). D) Visualization of the angle between BB and pBB. The data is plotted equivalent to B with the mean angle of 48.5° and the standard deviation of 39.8° indicated as described before. E) Histogram illustrating the distribution of the data points shown in D (bin size = 10°).

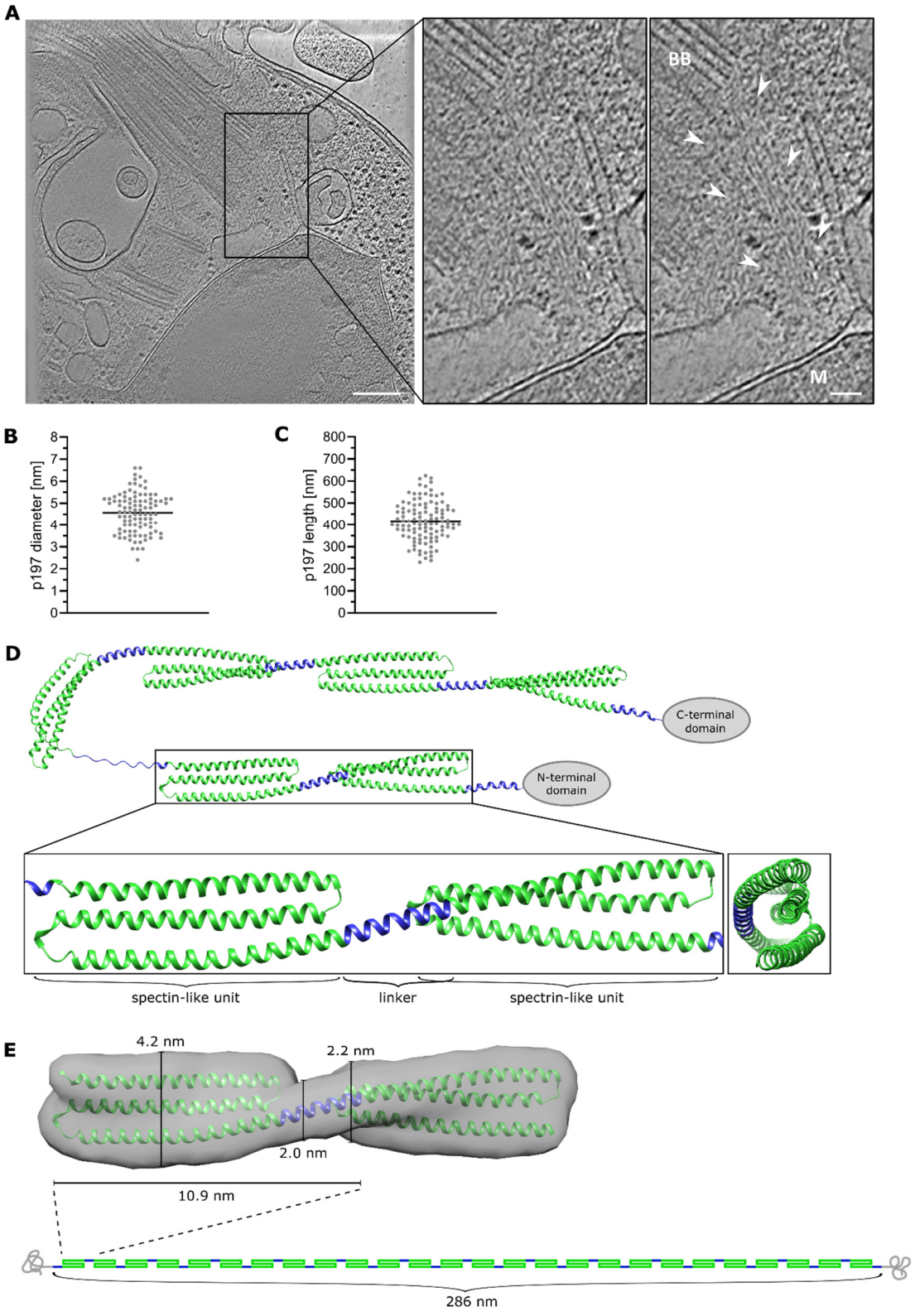

799 Figure 6: Structural analysis of individual p197 filaments.

800 A) Exemplary image of the p197 filaments as observed in cryo-electron tomograms. Overview of the
801 TAC area on the left (scale bar: 200 nm) and a magnified view of the exclusion zone in the middle.
802 The picture on the right shows the same zoom-in, with additional annotations: M, mitochondrion;
803 BB, basal body; scale bar: 50 nm. Arrowheads point at the region where p197 is clearly visible. Full
804 tomogram shown in Movie S 7; zoom-in of the EZF shown in Movie S 8. B) Summary of

measurements on filament diameter collected from a total of ten tomograms with ten measurements per tomogram. C) Summary of measurements of filament length collected on a total of 22 tomograms with five measurements per tomogram. Individual filaments were traced manually, by following them across the 3D volume. D) Structure of the repeat section of p197 (six repeats) as predicted by AlphaFold2 (top panel, (Jumper et al., 2021)). Repetitive coiled coil structures (spectrin-like units) are depicted in green, while linker regions are shown in blue. The N- and C-terminal domain are represented schematically, as these areas of the protein were poorly resolved in the prediction. A subset of two spectrin-like units connected with the typical α-helical linker are shown and labelled in the bottom panel. The panel on the bottom right shows the top view onto the same subsection of the protein. E) (top) modelled substructure of two spectrin-like units in a density map of 1.5 nm resolution. Model diameters were measured and to range from 2.2 – 4.2 nm in the spectrin-like unit and down to 2 nm in the linker region. Based on the model, filament rise per spectrin-like unit plus linker is 10.9 nm. (bottom) schematic representation of full length p197, consisting of 26 spectrin-like units that are interspaced by the α-helical linker. The repetitive stretch is connected to the N- and C-terminal domains with the same α-helical linker. Total predicted length of the modelled protein domain is 286 nm.

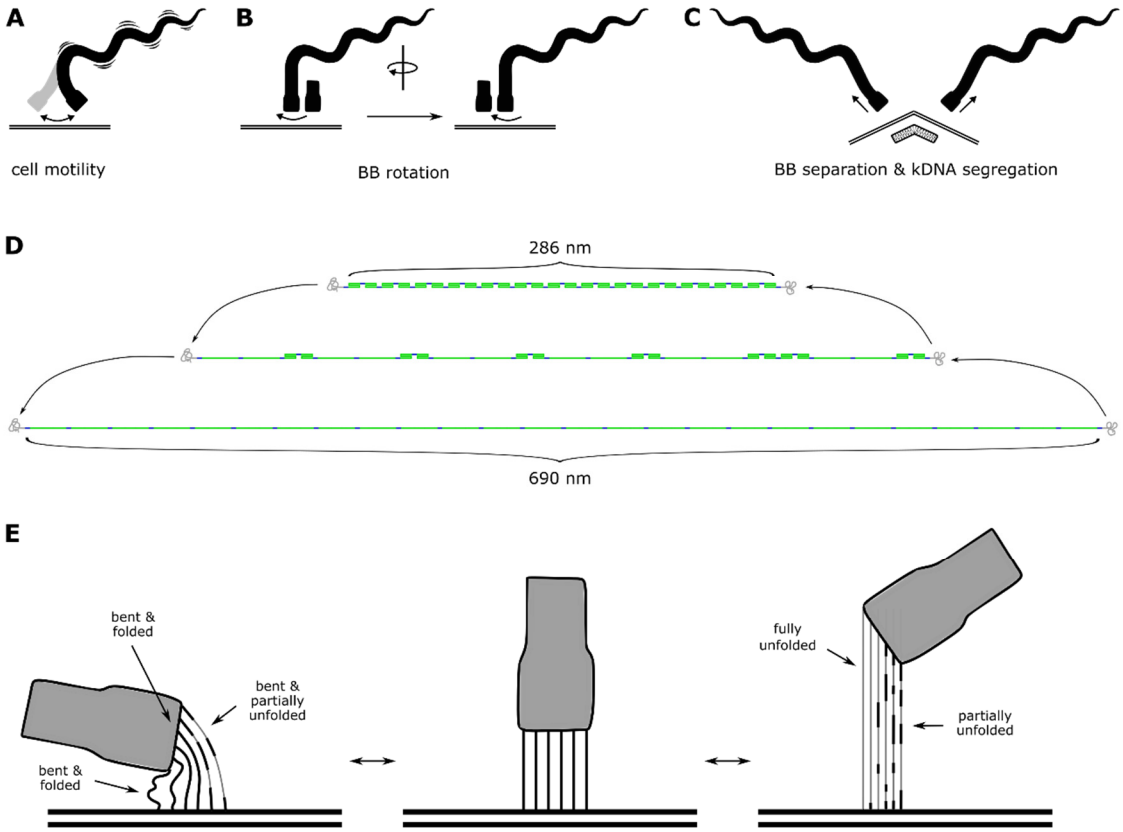

Figure 7: Cell motility and cell cycle dynamics impose mechanical forces on p197 that result in the reversible unfolding of spectrin-like units.

A) – C) Sources of BB/pBB movement relative to the OMM. The EZFs must withstand these movements. A) Being the base of a motile flagellum, the mature BB is subject to slight but constant tumbling movements. B) The freshly matured BB has been shown to rotate around its maternal BB to relocate to a position posterior of the maternal BB (Vaughan & Gull, 2016). C) kDNA segregation depends on the separation of the BBs prior to cytokinesis (Ogbadoyi et al., 2003). A stable connection between the BBs and the kDNA is essential for kDNA segregation. D) The effects described in A) – C) impose varying levels of mechanical force on p197. Individual p197 molecules will release spectrin-like units from their coiled coil assembly to account for BB/pBB movements. Upon rapprochement of the BB/pBB to the OMM, the tension is reduced, allowing spectrin-like units to fold back into the relaxed, coiled coil conformation. In its extremes, the repeat section extends from 286 nm (relaxed state) to a maximum of 690 nm (fully extended state). E) Overview of different positional arrangements of the BB towards the mitochondrial membranes. p197 responds to the varying distance between the BB and the OMM by bending and (un)folding in respect to the level of mechanical force imposed to the individual filament.

Supplementary Figures

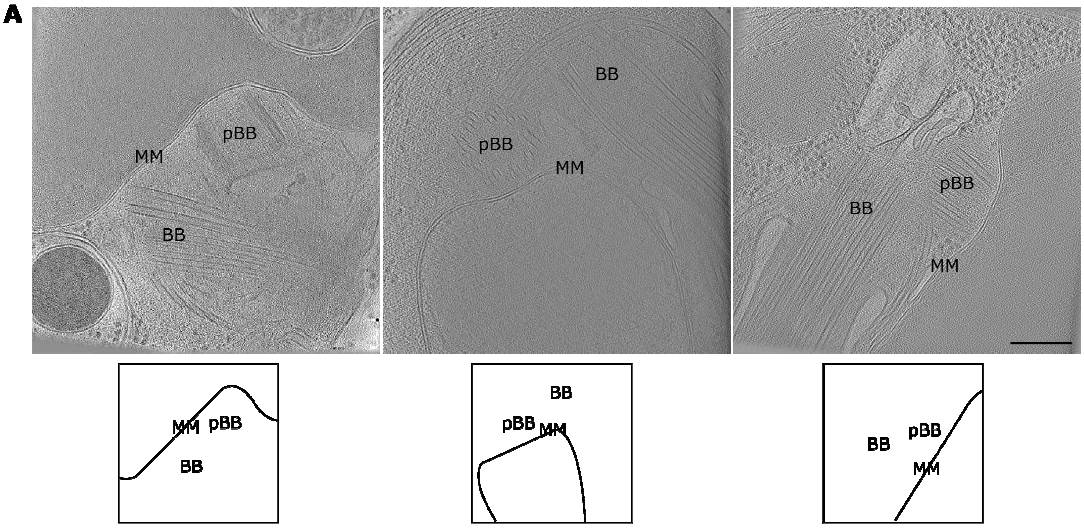

Figure S 1: The EFZ allow for a wide range of orientations of the basal bodies with respect to the mitochondrial membranes

A) (top) Representative tomographic slices demonstrating the diversity of orientations observed among the relevant structures (bottom). For visualization purposes, schematic representations of the basal body (BB), pro-basal body (pBB) and the mitochondrial membranes (MM) are depicted on the bottom of each tomographic slice.

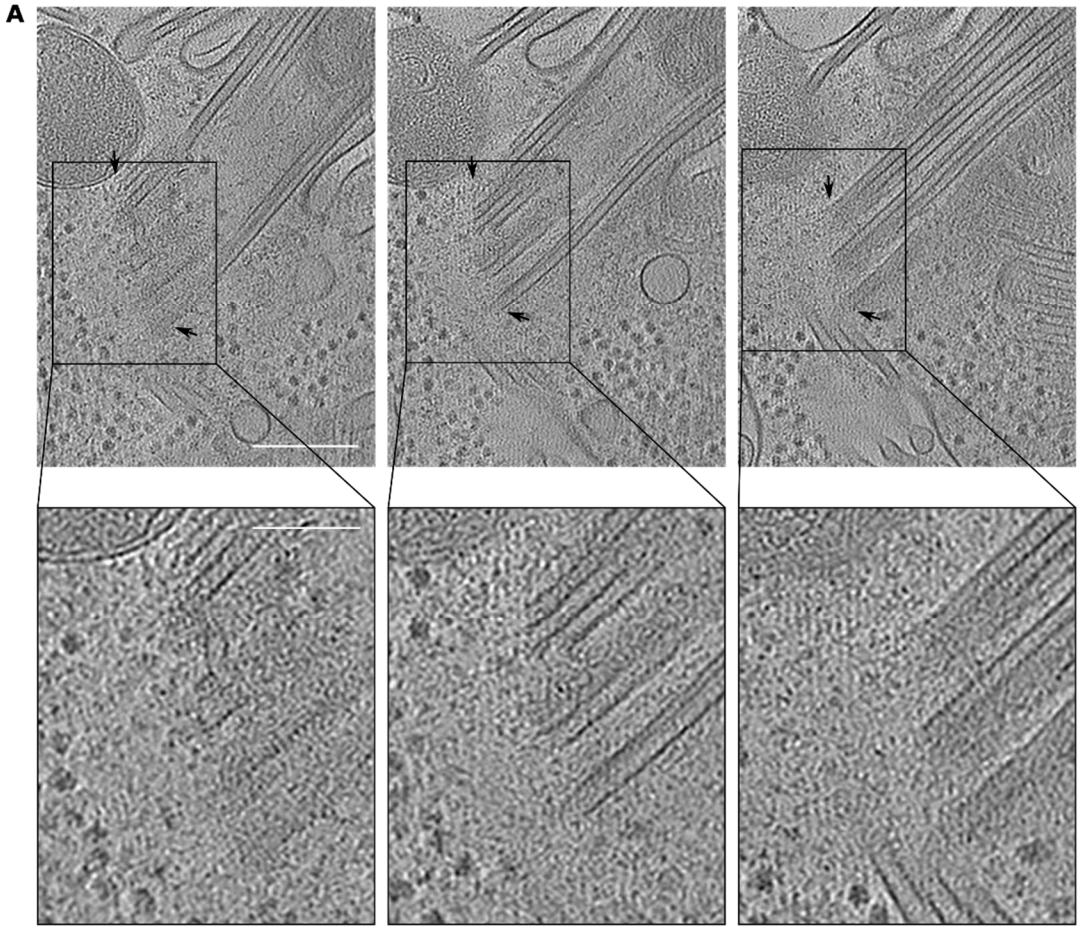

Figure S 2: tdzoids do not contain any EZFs.

A) To verify that the filaments we describe as EZFs are indeed part of the TAC, we performed cryo-ET on Tbcentrin4 p197 double RNAi cells (tdzoids). These cells are depleted of p197 and therefore also lack any downstream TAC components. The tomographic images depicted in the top row each show a 10-slice maximum intensity projection of a tomogram denoised with cryo-CARE (Buchholz et al., 2019). The image stacks are taken at three different heights along the cross-section of the mature BB (increasing z-height from left to right). Arrows point at the proximal face of the BB, where we the EZFs emanate in regular zoids. Scale bar: 200 nm. The bottom row shows zoom-ins at the region proximal to the BB. Scale bar: 100 nm.

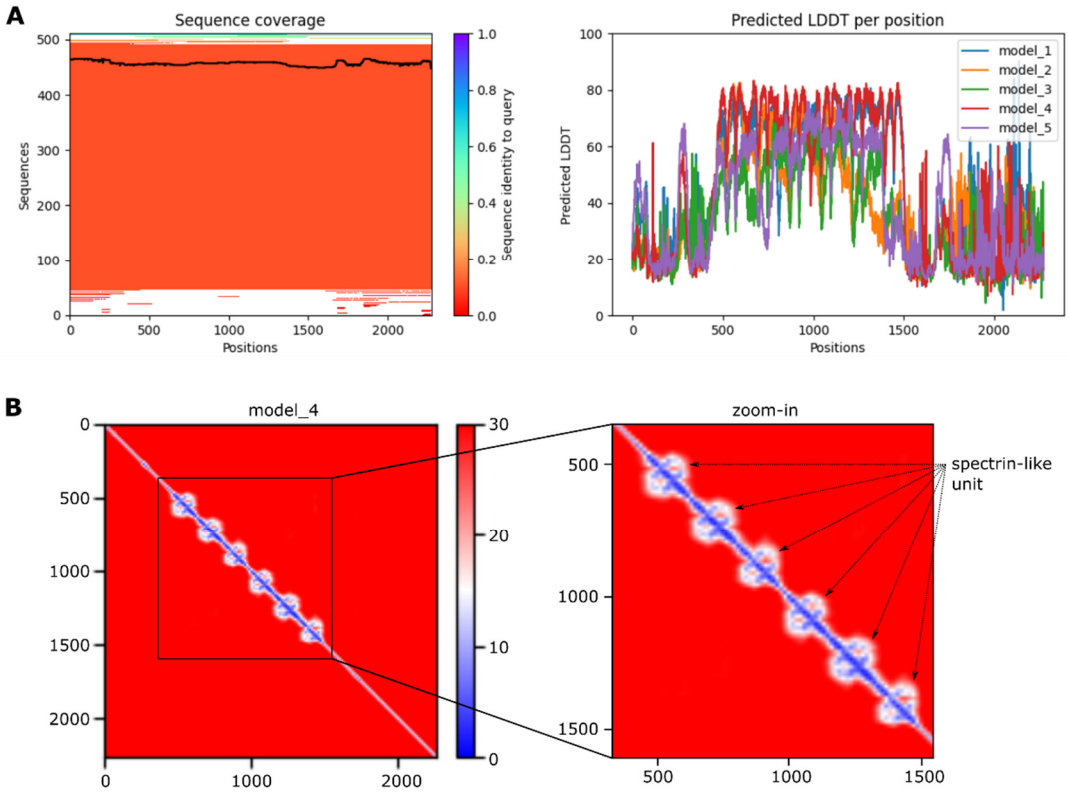

Figure S 3: Predictive scores of the AlphaFold2 prediction of the shortened p197-6Rep sequence.

A) Sequence coverage and local distance difference test (LDDT) plot of the AlphaFold2 (Jumper et al., 2021) run of a shortened version of p197 consisting of the N-terminal domain, six repeats and the C-terminal domain. Model_4 was selected for further analysis, as it scores highest in LDDT of the repeat section of the protein. B) Predicted aligned error (PAE) plot of the full sequence prediction (left) and zoom-in into the repeat section of model_4.

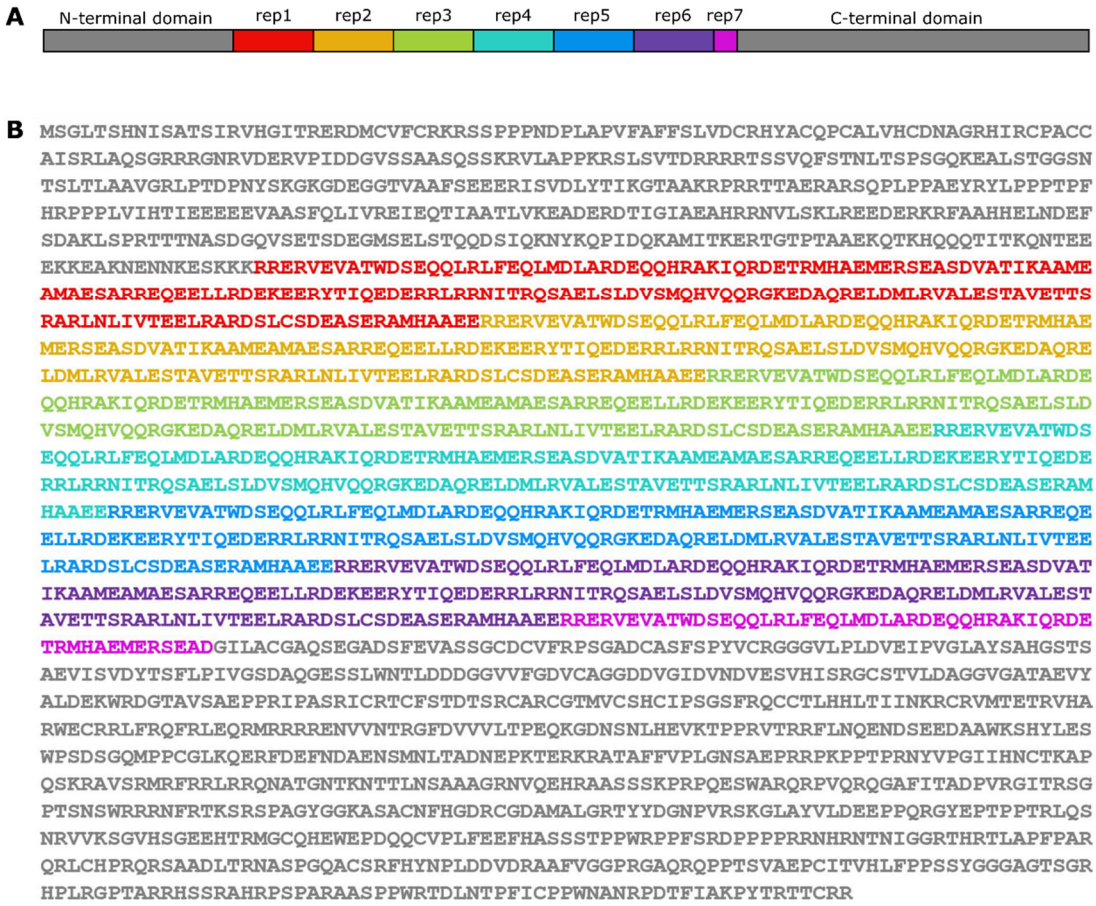

Figure S 4: Sequence composition of the truncated version of p197 as used for modelling.

A) schematic overview of the construct analysed AlphaFold2. N- and C-terminal domain are depicted in grey; sequence repeats 1 – 6 (rep1 – rep7) are shown in red, orange, green, cyan, blue, purple and pink. Repeat 7 is an incomplete repeat consisting of the first 53 amino acids of the sequence of repeats 1 – 6. B) sequence of the construct analysed in AlphaFold2. Colors match the colors in A.

Supplementary Movies

Movie S 1: Overview of the cryo-electron tomogram shown in Figure 2 A. Scale bar: 100 nm.

Movie S 2: Overview of the cryo-electron tomogram shown in Figure 3 A (left). Scale bar: 100 nm.

Movie S 3: Overview of the cryo-electron tomogram shown in Figure 3 A (right). Scale bar: 100 nm.

Movie S 4: Animation of the model shown in Figure 3 C (left). Scale bar: 200 nm.

Movie S 5: Animation of the model shown in Figure 3 C (left). Scale bar: 200 nm.

Movie S 6: Overview of the cryo-electron tomogram shown in Figure 4 A. Scale bar: 200 nm.

Movie S 7: Overview of the cryo-electron tomogram shown in Figure 6 A. Scale bar: 100 nm.

Movie S 8: zoom-in of the exclusion zone of the cell shown in the cryo-electron tomogram in Figure 6 A. Scale bar: 50 nm.